CHAPTER 5

Techniques for Earthquake Ground-Motion Calculation with Applications to Source Parameterization of Finite Faults

PAUL SPUDICH

Office of Earthquakes, Volcanoes and Engineering
United States Geological Survey
Menlo Park, California 94025

RALPH J. ARCHULETA

Department of Geological Sciences
University of California, Santa Barbara
Santa Barbara, California 93106

I. Introduction

The term "forward modeling" of earthquake ground motions refers to the calculation of the ground motions that would result from a given earthquake occurring in a specified geologic environment. Such forward modeling can be used to predict ground motions for engineering design purposes and to determine earthquake source parameters by iterative modeling of observed ground motions. In this chapter we examine how ground motions can be calculated at locations near to large earthquakes, in which case the source cannot be approximated as a point in space or time. We will also show how these forward modeling techniques allow one to determine the evolution of slip on a fault in a manner consistent with observed ground-motion data. Our emphasis will be upon calculation techniques that have been used in geologic structures that vary in at least one dimension. Consequently, we will not dwell on examples of forward

modeling of ground motions in uniform whole space or half-space velocity structures, except when they illustrate a principle applicable to more general velocity structures. We will concentrate on methods that are more rapid computationally than finite-element or finite-difference solutions to the problem. In addition we will emphasize techniques that model earthquakes as slip on fault surfaces, although volume sources will also be considered. We will present derivations of many of the relevant equations, although these derivations are intended only as tutorial sketches in which the most important concepts are emphasized and the details suppressed.

A. Classification of Methods

For the purpose of later discussion, it will be helpful to classify some of the methods used to calculate ground motions caused by extended seismic sources. The main classification attribute will be whether point-source Green's functions are used and how they are used. Aside from illustrating the concepts behind the methods, this classification can be significant from a computational standpoint, depending upon the relative computational effort required to specify a source model and to propagate the resulting waves through the surrounding medium. Methods that use Green's functions that have been explicitly calculated will be called explicit Green's function integration methods. Methods called implicit Green's function integration methods will be those in which the Green's functions appear in the mathematics but are never actually calculated. Methods that do not use Green's functions at all will be called non-Green's function methods. The main difference between these methods is that for non-Green's function methods the action of the extended seismic source is inextricably linked to the propagation of the resulting waves to the observer. Every time the ground motions from a new extended source are desired, the entire calculation must be repeated. Examples of such work are the finite-element modeling of Archuleta and Frazier (1978) and the discrete wave number technique of Bouchon (1979). Explicit Green's function integration methods lie at the opposite end of the spectrum. In them, the wave propagation problem is solved once for a set of point sources, and these Green's functions are reused for every new extended source model. In implicit Green's function integration methods, the Green's functions appear in the mathematics, but there is no need ever to calculate them explicitly because of their simplicity.

B. Seismic Representation Theorems

A representation theorem is a mathematical statement that relates an observable quantity, such as ground motion, to the parameters of an

idealized model of a seismic source. The most commonly studied seismic sources are tectonic earthquakes, volcanic earthquakes, and explosions. Often earthquakes are idealized as dislocations on planar fault surfaces, and explosions are idealized as centers of compression, but these idealizations are simplifications of the actual situation. Explosions can result in the creation of permanent cavities and can be accompanied by nonlinear material behavior and shear deformation resulting from the relaxation of local tectonic stress. Earthquakes are similarly complex upon detailed examination of the source region. From mapping of surface rupture, geologic investigation of exhumed fault zones (Sibson, 1986), and exposures of source zones in mines (Gay and Ortlepp, 1974), we know that earthquakes can have regions in which the local rock deforms inelastically during the earthquake (White, 1973). They may have local volume changes (Gilbert and Dziewonski, 1975) possibly due to phase transitions or thermal expansion. The source zone generally has many internal surfaces across which slip occurs (Tchalenko and Ambraseys, 1970). These surfaces may or may not intersect each other. They may display roughness (i.e., deviation from a plane surface) on all spatial dimensions (Tchalenko, 1970; King, 1983). Dislocation on these surfaces may occur as cavitation and injection of fluids such as water vapor or magma (Julian, 1983). Frictional melting may take place on these surfaces during the earthquake (Sibson, 1980).

1. Volume Sources

Because actual earthquake and explosion sources show complexities that may not be properly represented by the simple idealizations mentioned earlier, we will start by discussing representation theorems valid for seismic sources occupying a volume. Such representations have already been used to calculate ground motions from an explosion (see, e.g., Bache *et al.*, 1982) but have not yet been applied to earthquakes.

Volume sources can be dealt with in two ways. The first of these uses the concepts of stress-free strain (Robinson, 1951) or stress glut (Backus and Mulcahy, 1976a). Backus and Mulcahy give a representation theorem valid for a source distributed in a volume V. The kth component of displacement at observation position $\mathbf{y}$ and time t is

$$u_k(\mathbf{y}, t) = \int_{-\infty}^{\infty} dt' \iiint_V \Gamma_{pq}(\mathbf{x}, t')\, \partial_{x_q} G_{kp}(\mathbf{y}, t - t'; \mathbf{x}, 0)\, dV, \qquad (1)$$

where $\mathbf{x}$ is a location within V, Γ is the stress glut characterizing the seismic source, and $G_{kp}(\mathbf{y}, t - t'; \mathbf{x}, 0)$ is the kth component of displacement at position $\mathbf{y}$ and time $t - t'$ caused by an instantaneous force of unit impulse applied in the p direction at position $\mathbf{x}$ and time $t = 0$ (i.e., the usual point-force Green's function), where the summation convention applies over repeated indices and where $\partial_{x_q} = \partial/\partial x_q$. The stress glut is related to

the stress-free strain tensor $\mathbf{e}^F$ by

$$\Gamma = \mathbf{C} : \mathbf{e}^F, \tag{2}$$

where $\mathbf{C}$ is the tensor of elastic constants.

To see how this representation could be used with a complicated source model, consider an initially quiescent "reference" earth model having known material properties and state of stress everywhere. For simplicity let us also assume that the stress–strain relation in our reference model is given by simple time-independent linear elasticity and that there is zero prestress. The Green's functions and elastic tensor in Eqs. (1) and (2) are those appropriate for the reference earth model. We characterize our source model by specifying the strain and stress fields $\mathbf{e}(\mathbf{x}, t)$ and $\boldsymbol{\sigma}(\mathbf{x}, t)$ everywhere within the source volume V. Note that $\mathbf{e}$ cannot equal $\mathbf{C} : \boldsymbol{\sigma}$; if it did, linear elasticity would prevail everywhere within the source volume, and no waves at all would be generated. Seismic waves are generated where the true stresses $\boldsymbol{\sigma}$ in our source model differ from the stresses $\mathbf{C} : \mathbf{e}$ that would be expected in our reference earth model. This difference is the stress glut:

$$\Gamma(\mathbf{x}, t) = \boldsymbol{\sigma}(\mathbf{x}, t) - \mathbf{C}(\mathbf{x}) : \mathbf{e}(\mathbf{x}, t). \tag{3}$$

Because linear elasticity is usually assumed to prevail in the reference earth model, the region where stress glut is nonzero is identical to the region in which inelastic deformation occurs. Hence, regions where inelastic deformation occurs can be regarded as sources of seismic waves.

An arbitrarily complicated seismic source can be described by specifying its associated stress and strain fields $\boldsymbol{\sigma}(\mathbf{x}, t)$ and $\mathbf{e}(\mathbf{x}, t)$. For realistic seismic sources specification of $\boldsymbol{\sigma}$ and $\mathbf{e}$ can be quite difficult, since the action of a seismic source is governed by numerous laws of physics whose solution can be a formidable mathematical or computational problem. We shall use the term "dynamic" source models to refer to those models in which the appropriate laws of physics have been solved to obtain physically self-consistent $\boldsymbol{\sigma}$ and $\mathbf{e}$. Models in which $\boldsymbol{\sigma}$ and $\mathbf{e}$ are chosen that do not satisfy the appropriate physical laws will be called "kinematic" models, since the motion of the source is specified. From a historical standpoint, the distinction between kinematic and dynamic sources is not very important for volume earthquake sources, because almost no kinematic volume sources have been used for earthquakes thus far. This distinction is much more important for surface sources, such as slip on infinitesimally thin fault surfaces.

A second representation theorem has been used by Bache *et al.* (1982) for a volume source. In their method the source is replaced by the displacements and tractions it causes on an arbitrary surface Σ enclosing the source (Fig. 1). These displacements and tractions can be calculated on

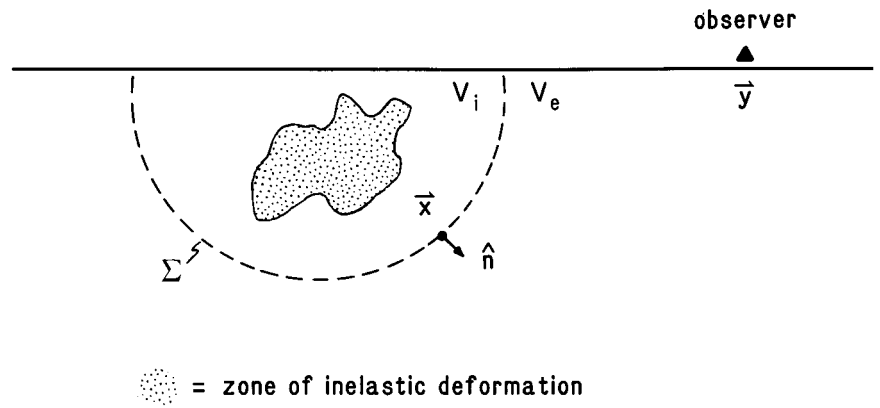

FIG. 1. Surface Σ separates the regions of purely elastic behavior V_e from a volume V_i containing all inelastic behavior; V_i can also contain elastic regions, and the exact position of the surface Σ is chosen for computational convenience. The action of the source is represented by the displacements and tractions it causes on Σ.

Σ for an arbitrarily complicated source by a finite-element or finite-difference method. Let us denote these displacements and tractions by $\mathbf{u}_s(\mathbf{x},t)$ and $\mathbf{T}_s(\mathbf{x},t)$. We use the material properties in V_e to define our reference earth model [see Bache *et al.* (1982) for details regarding the selection of a reference earth model], and we denote the Green's functions appropriate for this model by the vector $\mathbf{G}^j$, where the ith component of $\mathbf{G}^j$ is G_{ij}, as in Eq. (1), and j is the point-force direction. $\mathbf{G}^j$ causes tractions $\mathbf{T}^j$ across a surface with normal $\hat{\mathbf{n}}$. We then have the representation

$$u_j(\mathbf{y},t) = -\int_{-\infty}^{\infty} dt' \iint_{\Sigma} \mathbf{G}^j(\mathbf{x},t';\mathbf{y},0) \cdot \mathbf{T}_s(\mathbf{x},t-t') - \mathbf{u}_s(\mathbf{x},t') \cdot \mathbf{T}^j(\mathbf{x},t-t';\mathbf{y},0)\, d\Sigma \tag{4}$$

for the geometry shown in Fig. 1. Both Eqs. (1) and (4) can be used for forward modeling of volume sources. If a finite-element or finite-difference method must be used to determine stress glut Γ_{pq} in Eq. (1), then Eq. (4) is probably a more simple representation to use. This is because Eq. (4) involves a surface integral rather than a volume integral. However, Eq. (1) is preferable for doing the inverse problem because its kernel contains the source term we would like to resolve.

2. Surface Sources

Beginning with Aki's (1968) analysis of the 1966 Parkfield, California, earthquake, almost all modeling of earthquake sources and ground motions

at local distances ($R < 200$ km) has made the rather restrictive assumptions that earthquakes occur as slip on a small number of infinitely thin, usually planar, fault surfaces, and that the slip direction is locally tangent to the fault surface. This model of earthquakes is mathematically and computationally much more convenient than a volume source model and has been adequate for obtaining a first-order understanding of the earthquake rupture process. It has been successfully used for waveform modeling of earthquake-generated ground motions at periods down to about $\frac{1}{5}$ of the faulting duration, which is approximately the length of the fault divided by the shear wave speed. In this chapter, we will concentrate on earthquake source models that make the surface source approximation, although we point out that the understanding of more realistic volume sources is a highly desirable and largely unpursued goal.

Neglecting the effects of self-gravitation and prestress, Backus and Mulcahy (1976b) show that the stress glut associated with a displacement discontinuity $\mathbf{s}$ on surface Σ is

$$\Gamma_{ij} = C_{ijkl} n_k s_l, \tag{5}$$

where $\hat{\mathbf{n}}$ is a unit vector normal to Σ pointing into the positive side of Σ, and the displacement discontinuity $\mathbf{s}$ is the difference in displacement between the positive and negative sides of the fault,

$$\mathbf{s}(\mathbf{x}, t) = \mathbf{u}(\mathbf{x}^+, t) - \mathbf{u}(\mathbf{x}^-, t), \tag{6}$$

where $\mathbf{x}$ is a point on surface Σ. Equation (5) is valid for displacement discontinuities both parallel and perpendicular to the fault. Inserting Eq. (5) into Eq. (1) gives the most commonly used representation

$$u_m(\mathbf{y}, t) = \int_{-\infty}^{\infty} dt' \iint_{\Sigma} C_{ijkl} n_k s_l \, \partial_{x_j} G_{mi}(\mathbf{y}, t - t'; \mathbf{x}, 0) \, d\Sigma, \tag{7}$$

which was presented by Maruyama (1963), Burridge and Knopoff (1964), and Haskell (1964). By using the reciprocity relation for Green's functions

$$G_{ij}(\mathbf{y}, t; \mathbf{x}, 0) = G_{ji}(\mathbf{x}, t; \mathbf{y}, 0), \tag{8}$$

Eq. (7) may be rewritten

$$u_m(\mathbf{y}, t) = \int_{-\infty}^{\infty} dt' \iint_{\Sigma} C_{ijkl} n_k s_l \partial_{x_j} G_{im}(\mathbf{x}, t - t'; \mathbf{y}, 0) \, d\Sigma. \tag{9}$$

The form of Eq. (7) is more intuitively satisfying than that of Eq. (9) because the Green's functions in Eq. (7) are those describing wave propagation from a point force applied on the fault surface to the observer location, whereas in Eq. (9) the point forces are applied at the observer location and the Green's functions are evaluated on the fault. However, Eq.

(9) is slightly more general than Eq. (7); Burridge and Knopoff (1964) derive Eq. (9) first and then obtain Eq. (7) by making an assumption of homogeneous boundary conditions. Moreover, Eq. (9) can be computationally more convenient than Eq. (7) depending upon the number of observation locations and the method for calculating Green's functions. For example, if a finite-element (FE) or finite-difference (FD) method is used to calculate Green's functions for a laterally heterogeneous seismic velocity structure, three Green's functions calculations must be performed for each observer location (one for each component m of ground motion), whereas straightforward application of Eq. (7) would require three separate calculations for each point on Σ. For a laterally homogeneous velocity structure, Archuleta and Day (1980) show that use of Eq. (9) necessitates only two FE or FD calculations, regardless of the number of observers, due to the invariance of the Green's function under horizontal translation and to the cylindrical symmetry of the geometry. Spudich and Frazer (1984) point out that use of Eq. (9) is advantageous when using ray theory Green's functions, since the required ray tracing can be accomplished by simple shooting from the observer to the fault rather than by the two-point ray tracing needed to shoot from a point on the fault to each observation point. However, Eq. (9) offers no computational advantages over Eq. (7) if the desired number of observation locations is very large or if the so-called spectral methods (Chapman, 1978) are used to calculate Green's functions, because in these methods equal computation time is needed for the case of a single source depth and multiple receiver depths and vice versa. We note that Eq. (8) may also be applied to our volume source representations Eqs. (1) and (4).

Before proceeding, it is worthwhile to clarify some terminology. The terms "source" and "receiver" are ambiguous when applied to Eq. (9) because of the use of Green's function reciprocity. We will always use the term "observer location" or something similar to refer to point $\mathbf{y}$ in Eq. (9), which is the place where ground motions caused by the extended seismic source are to be evaluated. We will only use the term "receiver" to correspond to the first argument of either Green's function in Eq. (8). Hence, $\mathbf{y}$ is the receiver in Eq. (7) and $\mathbf{x}$ is the receiver in Eq. (9). The term "source" will refer to the location of the point force or point-moment tensor when discussing Green's functions and will otherwise denote the region of nonzero stress glut.

In order to simplify Eq. (9) further, we note that the stress tensor σ_G associated with the Green's function in Eq. (9) is

$$\sigma_G^m(\mathbf{x}, t; \mathbf{y}, 0) = C_{ijkl}(\mathbf{x})\, \partial_{x_j} G_{im}(\mathbf{x}, t; \mathbf{y}, 0), \tag{10}$$

where m is the point-force direction. Hence the associated traction $\mathbf{T}^m$

exerted across the fault surface with normal $\hat{\mathbf{n}}$ is

$$\mathbf{T}^m(\mathbf{x}, t; \mathbf{y}, 0) = \hat{\mathbf{n}} \cdot \boldsymbol{\sigma}_G^m \tag{11}$$

and Eq. (9) may be written (Spudich, 1980) as

$$u_m(\mathbf{y}, t) = \int_{-\infty}^{\infty} dt' \iint_{\Sigma} \mathbf{s}(\mathbf{x}, t') \cdot \mathbf{T}^m(\mathbf{x}, t - t'; \mathbf{y}, 0)\, d\Sigma. \tag{12}$$

If we denote the Fourier transform of $f(t)$ by

$$f(\omega) = \int_{-\infty}^{\infty} f(t) e^{-i\omega t}\, dt, \tag{13}$$

then the frequency domain version of Eq. (12) is

$$u_m(\mathbf{y}, \omega) = \iint_{\Sigma} \mathbf{s}(\mathbf{x}, \omega) \cdot \mathbf{T}^m(\mathbf{x}, \omega; \mathbf{y}, 0)\, d\Sigma. \tag{14}$$

Although Eq. (14) is perfectly valid, the slip functions of greatest seismological interest have static offsets, and consequently their Fourier transforms are undefined. If we denote temporal derivations with an overdot, then slip velocity is $\dot{\mathbf{s}}$, and Eq. (14) may be written in a form more advantageous for numerical evaluation as

$$\dot{u}_m(\mathbf{y}, \omega) = \iint_{\Sigma} \dot{\mathbf{s}}(\mathbf{x}, \omega) \cdot \mathbf{T}^m(\mathbf{x}, \omega; \mathbf{y}, 0)\, d\Sigma, \tag{15}$$

where $\dot{u}_m$ is the m component of ground velocity. The ground velocity time series may be obtained by inverse Fourier transformation of $\dot{u}(\omega)$. We have found it computationally most stable to obtain acceleration $\ddot{\mathbf{u}}(t)$ by inverse Fourier transformation of $i\omega\dot{\mathbf{u}}(\omega)$, and displacement $\mathbf{u}(t)$ by temporal integration of $\dot{\mathbf{u}}(t)$, thus avoiding difficulties with the $\omega = 0$ term. Although in later sections we will often refer to the slip function itself, it should be understood that, in practice, the slip rate function is used for computing ground motion when the method of calculation involves the frequency domain.

II. The Fault Surface Integral

At present there is no clearly preferred method for calculating ground motions in the near-source region of an earthquake. A variety of methods have been used. Each has its own range of validity, and almost all are computationally expensive. In this section we will review a number of the methods, explain the basic physics behind them, and point out their strengths and weaknesses.

From Section I.B, the basic integral to be evaluated is

$$\dot{u}(\omega) = \iint_{\Sigma} \dot{\mathbf{s}} \cdot \mathbf{T}\, d\Sigma. \tag{16}$$

Calculation of near-source ground motions is generally difficult because for geologically realistic situations both terms in the integrand are computationally expensive to obtain. For example, the slip-rate vector $\dot{\mathbf{s}}$ may be obtained for a fault having heterogeneous strength and stress drop by three-dimensional FD, FE, or boundary-integral calculations, as discussed by Mikumo in Chapter 3 of this volume. The formidable problem of wave propagation in laterally heterogeneous media must be solved to obtain the traction Green's functions. If the surface integral in Eq. (16) is performed numerically and equal accuracy is desired for each frequency, the computational effort needed is proportional to the square of the frequency and to the cube of the frequency bandwidth desired in the calculated ground motions (we will elaborate on this statement later). Consequently, a number of approximations are often made to obtain $\dot{\mathbf{s}}$ and $\mathbf{T}$. In many cases, the particular approximations made to $\dot{\mathbf{s}}$ and $\mathbf{T}$ can interact to simplify the surface integral calculation. In the following sections, we will discuss some of these approximations.

A. Slip Rate Vector $\dot{\mathbf{s}}(\mathbf{x}, t)$ for Kinematic Models

In many ways specification of the slip rate vector is the central element of a kinematic faulting model. The slip rate vector represents one's understanding of the behavior of the earthquake rupture. Based on waveform matching of synthetic ground motion and real ground motion (see, e.g., Archuleta and Day, 1980; Olson and Apsel, 1982; Hartzell and Helmberger, 1982; Hartzell and Heaton, 1983, 1986; Archuleta, 1984), the behavior of the earthquake source is relatively well modeled for frequencies up to 1–2 Hz. Above these frequencies the source is not well understood deterministically, and normally a statistical approach is taken (Haskell, 1966; Aki, 1967; Boore and Joyner, 1978; Andrews, 1981; Izutani, 1981; Boatwright, 1982; Koyama, 1985). This lack of understanding of the high-frequency behavior of an earthquake source is one of the major obstacles to accurate prediction of ground motions above 1.0 Hz. In the following we consider rupture models that have been successfully used at frequencies $\leq$ 1.0 Hz. We have chosen to discuss the slip rate vector rather than the slip vector because its Fourier transform is well behaved, i.e., we do not have to take into account the static offset inherent in the slip vector itself (see Section I.B). The slip rate vector has components only in the fault plane for shear faulting. Thus, if one chooses the convenient basis vectors

$\hat{\mathbf{x}}_1$ and $\hat{\mathbf{x}}_2$ in the directions along strike and downdip, respectively, the slip rate vector will have strike-slip and dip-slip components $\dot{s}_1$ and $\dot{s}_2$, respectively. Some of the parameters needed to describe the slip rate depend on the function chosen for the slip rate. Other parameters, primarily the rupture time, are directly associated with the slip rate but are not dependent on the function itself.

The most common functional form for the slip rate, a rectangle function $\Pi(t)$ (Bracewell, 1965, p. 52), is the Haskell (1964) model in which the slip at a given $\mathbf{x}$ is a linear ramp with a rise time $\tau(\mathbf{x})$ (Fig. 2a). In order to allow for a propagating rupture, different points on the fault will slip at different times. Thus, each point on the fault has a rupture time $t_s(\mathbf{x})$ at which the slip initiates. This parameter enters naturally into the slip rate function

$$\dot{\mathbf{s}}(\mathbf{x}, t) = [a_1(\mathbf{x})\hat{\mathbf{x}}_1 + a_2(\mathbf{x})\hat{\mathbf{x}}_2]\Pi\{[t - t_s(\mathbf{x})]/\tau(\mathbf{x})\}, \qquad (17)$$

where a_1 and a_2 are components of the slip-rate vector. This description of the slip rate depends on four basic parameters, $a_1(\mathbf{x}, t)$, $a_2(\mathbf{x}, t)$, $\tau(\mathbf{x})$, and $t_s(\mathbf{x})$.

There are a number of variations of the Haskell model. For example, Hartzell and Helmberger (1982) use a triangular slip rate function to compute synthetics for the 1979 Imperial Valley, California, earthquake. Because dynamic models of a propagating stress relaxation (Madariaga, 1976; Archuleta and Frazier, 1978; Day, 1982) show that the functional form of the slip rate closely resembles the form derived by Kostrov (1964) for a self-similar propagating stress drop, the Kostrov model (Fig. 2b) has become a prominent alternative to the Haskell model. Archuleta and Hartzell (1981), Boatwright (1981), and Campillo and Bouchon (1983) have

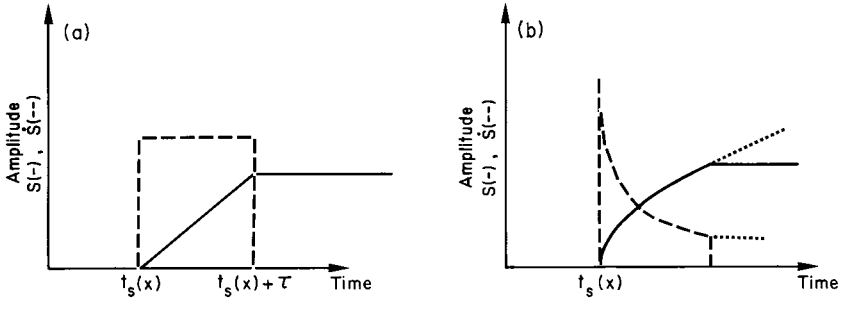

FIG. 2. Functional forms for slip and slip rate. (a) The Haskell slip function (solid line) and the slip rate function (dashed line) are shown for source point at position $\mathbf{x}$. The rupture time function $t_s(\mathbf{x})$ and the rise time $\tau(\mathbf{x})$ are shown. (b) The modified Kostrov slip and slip rate functions are shown as the solid and dashed lines, respectively. The dotted line indicates the shape of the Kostrov functions before modification.

used a modified Kostrov function to generate high frequency synthetic seismograms. Although the functional forms of the Haskell model and the Kostrov model are quite different, the number of parameters needed to specify each is the same. Although the computation is not reduced, one could argue that the Kostrov dislocation better represents the physics of the earthquake mechanism. If only low frequencies are being considered, the two dislocation models are approximately the same because the singularity in the Kostrov slip rate at the arrival time of the rupture is eliminated by low passing the slip rate function (Archuleta and Hartzell, 1981). Both models are kinematic in that the dislocation is specified without regard to the forces acting in the process.

Given that the slip rate is specified with four parameters, a crucial observation is that two of the parameters $\dot{s}_1$ and $\dot{s}_2$ are linearly related to the ground motions, while τ and t_s are not (Archuleta, 1984). This feature of the parameterization became the critical element in Archuleta's attempt to model the faulting of the 1979 Imperial Valley earthquake. He found that variations in the rupture time t_s had a pronounced effect on the synthetic seismograms, whereas variations in the rise time τ and the slip rate amplitudes s_1 and s_2 cause either small or predictable changes. The effect on the synthetics of changing the slip rate amplitude is strongly governed by geometrical attenuation ($\approx R^{-1}, R^{-2}, R^{-4}$ for the far-, intermediate-, and near-field terms, respectively, where R is the distance between the observer and the point on the fault). Thus, any change in the slip rate amplitude affects most the synthetics at stations closest to where the change in slip rate amplitude was made. This is not the case with the rupture time or the rise time. However, as Anderson and Richards (1975) showed, it takes a 300% change in rise time to compensate for a 17% change in rupture time. In section II.C.1 we show why rupture time variations have such a strong effect, which has also been discussed by Spudich and Oppenheimer (1986).

A primary effect is that when doing forward modeling of data, changing the slip rate amplitudes while holding the rupture time fixed may produce a better fit, i.e., one finds a local minimum of misfit in model space. Finding the global minimum, or even recognizing it, given that two of the parameters in the model are nonlinearly related to the data is a major unanswered question in forward modeling. This problem has been avoided to some extent in ground motion studies using linear inverse techniques by choosing a parameterization of $\dot{\mathbf{s}}(\mathbf{x}, t)$ in which $t_s(\mathbf{x})$ does not appear explicitly. Spudich (1980) represented $\dot{\mathbf{s}}$ as an arbitrary continuous function of position and time, in which case Eq. (15) is completely linear in $\dot{\mathbf{s}}$. Using Spudich's parameterization, however, does not necessarily lead to solutions for $\dot{\mathbf{s}}$ that show a conspicuous rupture front. To alleviate this problem,

Olson and Apsel (1982) and Hartzell and Heaton (1983, 1986) used a different, more restrictive parameterization of $\dot{s}$ that preserved the linearity of the problem while constraining all the slip to occur within a time window chosen *a priori*.

B. Comments on Green's Functions Pertaining to the Fault Surface Integral

The calculation of Green's functions in various types of earth models has been a fundamental research area in seismology, and an enormous body of literature deals with the subject. In this section, we will limit ourselves to describing some of the methods that have been used for extended-source calculation, and we will comment primarily on those aspects of the methods that have a practical relevance in such calculations. These aspects are (1) the accuracy for realistic earth models, (2) the computational effort required by each, and (3) any structure in the mathematical expressions that facilitates the inclusion of an extended seismic source.

1. General Comment on Accuracy

For the modeling of observed earthquake seismograms, or for prediction of ground motions in a specific region, the first factor limiting the accuracy of any Green's function calculation is simple ignorance of the earth structure at the site. In order to calculate Green's functions accurately at 5 Hz for a particular region, it is necessary to know the 3D shear-velocity structure on a scale of a few hundred meters both horizontally and vertically. Since such a detailed knowledge of the earth's velocity structure may not be available in the near future, calculations of ground motions for real world situations are predestined to have errors. To our knowledge, no one has yet attempted to estimate these errors and carry them along as uncertainty estimates in subsequent calculations. Estimation of these errors would be relatively easy if microearthquake recordings were available in the study region. One could simply examine the spectrum of the difference between the observed microearthquake seismograms and synthetic seismograms calculated in the identical source–observer geometry for point dislocations. For frequencies below the microearthquake's corner frequency, the synthetic point-dislocation seismograms should match the observed seismograms. Probably it would be observed that the difference between the observed and synthetic seismogram spectra would increase as a function of frequency, corresponding to our progressively less accurate knowledge of earth structure on decreasing length scales. If quantitative measurements of these discrepancies were available, they could be used to estimate uncertainties in both forward modeling and inverse modeling of earthquake seismograms (Spudich, 1980).

A related approach was used by Archuleta (1984) in modeling the 1979 Imperial Valley earthquake seismograms. The shear wave velocity structure he used for calculating his Green's functions had been altered by trial-and-error modeling to improve the agreement between predicted ground motions and those observed for an aftershock of the 1979 event.

Another approach to the problem of inaccurate Green's functions is to use microearthquake seismograms as point dislocation Green's functions (Hartzell, 1978). Below the microearthquake corner frequency, these seismograms are exactly the Green's functions desired. A large amount of work has been done recently using this promising technique (Kanamori, 1979; Hartzell, 1982; Irikura, 1983; Imagawa *et al.*, 1984; Munguia and Brune, 1984; Joyner and Boore, 1986), which will not be reviewed in this chapter. The main impediments to the use of this idea are that at present there are generally not enough microearthquake records available to simulate the rupture of a large fault, and in many cases it is desired to calculate ground motions at frequencies above the microearthquake corner frequencies, in which case the question of earthquake scaling relations enters the picture. We note that Hartzell (1978) used four aftershocks of the 1940 El Centro earthquake to simulate the mainshock record, and the simulation worked very well at periods of 5 sec and longer. This is quite a different style of simulation than the high-frequency syntheses of Irikura (1983). A second factor, related to the general question of accuracy of theoretical Green's functions, is an entirely subjective question, namely, what attributes of the ground motion are important to calculate accurately? If the ground motion calculation is being done to aid in the engineering design of a structure, it may be that it is most important to calculate peak ground velocity accurately, or perhaps the total duration of long-period ground motion, or the root-mean-square acceleration. Considerations like these definitely affect the choice of a Green's function calculation method. For example, close to a fault the peak ground velocities are generally caused by the direct S wave, so that use of simple ray theory Green's functions may be ideal for such calculations (Spudich and Frazer, 1984). On the other hand, at larger distances the duration of long-period motion is generally related to surface wave excitation, and use of ray theory Green's functions to predict the duration of long-period motions at large distances would be an utter disaster. In the remainder of this chapter, it is presumed that the limitations of the various Green's function methods are known.

2. Green's Functions in 2D and 3D Media with Arbitrary Velocity Structure

Currently, FE and FD methods are the only techniques available that can be used to calculate complete Green's functions, i.e., Green's functions containing all possible body and surface waves in general, laterally varying

velocity structures. The chief limitation of such techniques is that the computational effort required for 3D models is proportional to f_{max}^4, where f_{max} is the maximum frequency of interest in the calculation. The exponent of 4 results from the necessity of using a number of mesh points per linear distance that is proportional to frequency, and a time step that is inversely proportional to frequency. In addition, the needed storage goes up as f_{max}^3. Because of the large computational effort, FE and FD methods have not been used (to our knowledge) for ground motion calculations in 3D, laterally varying media. An additional characteristic of these methods is that the Green's functions they generate are specified as the motions of a given set of mesh points, meaning that integrals of quantities like $\mathbf{s} \cdot \mathbf{T}$ must be done purely numerically.

If only body waves are desired in laterally varying structures, considerable work that is applicable to the extended source problem has been done on asymptotic ray theory and related methods such as Gaussian beams [see Červený and Klimeš (1984), and other articles in the same issue]. The chief advantages of ray-based methods are their rapidity of calculation (which is independent of frequency), their accuracy at high frequency (except for the omitted waves, of course), and the simple form of the Green's functions, consisting primarily of propagating delta functions. As Bernard and Madariaga (1984) and Spudich and Frazer (1984) have shown, this simplicity in the Green's functions greatly simplifies the fault surface integral and facilitates their use with extended seismic sources.

Another Green's function method that may have great potential for handling topographic effects and scattering by basins is the use of ray theory in conjunction with the Kirchhoff–Helmholtz theory (Frazer and Sen, 1985; Sen and Frazer, 1985). Such a method is excellent for the reflection or transmission of body waves at irregular interfaces because it includes diffractions. In addition, it could be very easily used with extended sources by employing the isochrone integration approach of Bernard and Madariaga (1984) and Spudich and Frazer (1984). Such an approach would necessitate the use of isochrone integration on multiple surfaces of integration, as in Haddon and Buchen (1981), with one being the fault and the others being the base of the basin, etc.

3. Laterally Homogeneous Media

Most ground motion calculations for extended seismic sources have been performed in laterally homogeneous media because the theory for Green's functions has been most fully developed for such media, and because it is computationally feasible to calculate complete synthetic seismograms for such media on a routine basis. In this section, we will concentrate primarily on methods for complete synthetic seismograms. In most places the earth's

material properties vary most strongly with depth, so that the assumption of lateral homogeneity seems reasonable. However, no one, to our knowledge, has ever examined quantitatively the degrees of misfit between real observed point-source seismograms and theoretical Green's functions calculated for a laterally homogeneous approximation to the local velocity structure.

The cylindrical symmetry and translational invariance of laterally homogeneous earth structures lead to simplifications of the mathematical expressions for the Green's functions. These simplifications have only partially been exploited to ease the integration of $\mathbf{s} \cdot \mathbf{T}$ over the fault surface. Before we can describe how the assumption of cylindrical symmetry interacts with integration of the Green's functions over the fault surface, it is necessary to present some of the mathematics describing waves in laterally homogeneous media. For simplicity and consistency of notation, we will refer primarily to Kennett (1983), who elaborates on the mathematics and gives proper credit to the original authors. The reader may also find Spudich and Ascher (1983) helpful.

a. Arbitrary Variation of Velocity with Depth Using a 2D Finite-Element Solution. While it is possible to use a 3D FE calculation to obtain Green's functions for a laterally homogeneous medium, Day (1977) has shown how Green's functions for the 3D geometry can be obtained from a less expensive 2D FE calculation in depth and epicentral distance. The advantages of his technique, aside from the obvious reduction of a 3D to a 2D calculation, are that Green's functions are obtained on a dense grid of points facilitating integration over a seismic source, and an arbitrary variation of velocity with depth is allowed in the medium. The basic idea of the method is that the displacements and stresses in an axisymmetric medium can be expanded in a Fourier series over azimuthal angle ϕ. For example, displacement $\mathbf{u}$ can be expanded

$$\mathbf{u}(r, z, \phi, t) = \sum_n \mathbf{U}(r, z, t, n) e^{in\phi}, \tag{18}$$

and the stresses can be expanded similarly. For each azimuthal order n, the expansion coefficient $\mathbf{U}$ can be obtained by a 2D FE calculation (see Day, 1977, for details). For a vertical point-force source, $\mathbf{U} \neq 0$ only for the $n = 0$ term, and for a horizontal point force $\mathbf{U} \neq 0$ only for $n = 1$. Hence, point-force Green's functions can be obtained for receivers at every point in a 3D axisymmetric medium by solution of two 2D FE calculations. Green's functions calculated in this manner were used by Archuleta and Day (1980) to do forward modeling of the 1966 Parkfield, California, earthquake.

b. Arbitrary Variation of Velocity with Depth Using Other Methods. By Fourier transformations of field quantities over azimuthal order, Day (1977)

reduced a 3D problem to a series of 2D problems. By performing a Bessel transform over epicentral distance, the problem can be reduced further to a series of 1D problems. This is the most common approach to laterally homogeneous problems. Its advantage for extended source calculations is that the horizontal variation of Green's functions can be expressed analytically instead of purely numerically.

In a cylindrical coordinate system (r, ϕ, z), the Fourier transform of displacement and z component of stress can be expanded as

$$\mathbf{u}(r, \phi, z, \omega) = \int_0^\infty k \sum_n [U\mathbf{R}_k^n + V\mathbf{S}_k^n + W\mathbf{T}_k^n]\, dk, \tag{19}$$

and

$$\boldsymbol{\sigma}_z(r, \phi, z, \omega) = \int_0^\infty k \sum_n [P\mathbf{R}_k^n + S\mathbf{S}_k^n + T\mathbf{T}_k^n]\, dk, \tag{20}$$

where k is a horizontal wave number and n is an integer. The mutually orthogonal vector surface harmonics $\mathbf{R}_k^n$, $\mathbf{S}_k^n$, and $\mathbf{T}_k^n$ are given by Kennett [1983, Eq. (2.48)], and they are proportional to $J_n(kr)e^{in\phi}$ and its derivatives, where J_n is the Bessel function of order n. The expansion coefficients $U, V, \ldots, T$ are functions of z, k, and ω that are to be determined. The continuity of $\mathbf{u}$ and $\boldsymbol{\sigma}_z$ with depth and the equations of motion yield the coupled differential equations for the coefficients $U, V, \ldots, T$,

$$d_z\mathbf{b}_P = A_P\mathbf{b}_P + \mathbf{F}_P, \tag{21}$$

and

$$d_z\mathbf{b}_H = A_H\mathbf{b}_H + \mathbf{F}_H, \tag{22}$$

where

$$\mathbf{b}_p = [U, V, P, S]^T, \tag{23}$$

and

$$\mathbf{b}_H = [W, T]^T. \tag{24}$$

Here, $\mathbf{F}_P$ and $\mathbf{F}_H$ are inhomogeneous source terms, the matrices A_P and A_H are given by Kennett (1983, p. 30), the T superscript indicates a transpose, and $d_z = d/d_z$. The system Eq. (21) corresponds to P–SV motion, and Eq. (22) corresponds to SH motion. We will refer to them as the P–SV and SH systems, respectively. Note that they are ordinary differential equations in one spatial dimension.

Because the elements of $\mathbf{b}$ are expansion coefficients for displacement and the z component of stress, as in Eqs. (19) and (20), $\mathbf{b}$ is often called the displacement–stress vector; $\mathbf{b}(z)$ is a continuous function of depth, and the propagator matrix $P(z_2, z_1)$ can be used to relate $\mathbf{b}(z_1)$ to $\mathbf{b}(z_2)$:

$$\mathbf{b}(z_2) = P(z_2, z_1)\mathbf{b}(z_1) \tag{25}$$

(Kennett, 1983, p. 40).

Typically, for a choice of parameters ω and k, the P–SV and SH systems are solved subject to a free-surface boundary condition, a radiation condition at large depth, and a particular inhomogeneous source term $\mathbf{F}(z)$. Although it is possible to represent an extended source through the term $\mathbf{F}(z)$, this is not the approach usually taken, although it would be worth investigating. Bouchon (1979) and Chouet (1987) include an extended source in a related manner, which will be described in Section II.C.4. The usual approach is to assume existence of a point source at depth z_s, which gives rise to a forcing term of the form

$$\mathbf{F}(z) = \mathbf{F}_1\delta(z - z_s) + \mathbf{F}_2 d_z\delta(z - z_s). \tag{26}$$

This source can be equivalently expressed as a discontinuity in $\mathbf{b}$ at depth z_s:

$$\mathbf{b}(z_s^+) - \mathbf{b}(z_s^-) = \mathbf{F}_1 + \omega A\mathbf{F}_2. \tag{27}$$

Kennett (1983, p. 95) gives expressions for the discontinuity in $\mathbf{b}$ caused by a point moment-tensor source. An alternate approach is to set $\mathbf{F}(z) = 0$ for all $\mathbf{z}$ and solve the P–SV and SH systems with a given traction boundary condition at $z = 0$ (Spudich and Ascher, 1983; Olson *et al.*, 1984). This procedure yields $\mathbf{b}$ at all depths for a surface source, and the spatial reciprocity relation for Green's functions can then be used to derive the free-surface displacements caused by buried sources.

Thus far we have been working in the frequency domain. Expansion of displacement and stress analogous to Eqs. (19) and (20) can be written in the time domain [see, e.g., Olson *et al.*, 1984, Eq. (2.7)], and the time-domain versions of Eqs. (19) and (20) are given by Alekseev and Mikhailenko [1980, Eqs. (16–18)] and Olson *et al.* [1984, Eqs. (2.8a–2.8c)]. These are partial differential equations in the (z, t) domain. Once Eqs. (21) and (22), or their time domain analogs, are solved for U, V, and W, the medium displacements are obtained by evaluation of Eq. (19).

When used to calculate Green's functions, the methods of Alekseev and Mikhailenko (1980), Spudich and Ascher (1983), and Olson *et al.* (1984) are in some ways well suited and in other ways poorly suited for extended seismic source calculations. Each of the methods solves the P–SV and SH systems on a dense grid of points in depth, which is very useful because the traction vector $\mathbf{T}$ must be known over the entire source. On the other hand, the computational effort they require rises very rapidly with frequency, limiting their utility to frequencies of a few hertz or less.

If complete seismograms are desired in the frequency band $(0, f_{\max})$, then the computational effort C required by all these methods scales like

$$C \approx n_k n_f n_z \text{ (or } n_k n_t n_z) \approx f_{\max}^3,$$

where n_k, n_f, and n_t are the number of wave numbers, frequencies, and time steps, respectively, for which the P–SV and SH systems are solved, and n_z is the number of mesh points needed in depth to solve each system. Here, C is proportional to $f_{\max}^3$, for the several reasons. The requirement of complete seismograms implies the use of waves having all slownesses from zero to some maximum slowness $p_{\max}$ usually greater than the slowness of the fundamental Rayleigh mode. Hence, the P–SV and SH equations must be solved for a range of wave numbers running from 0 to $k_{\max} = 2\pi p_{\max} f_{\max}$. If the wave number sampling scheme is independent of frequency, as it is in Alekseev and Mikhailenko (1980), Spudich and Ascher (1983), and Olson *et al.* (1984), then the number of wave number sample points for which the P–SV and SH equations must be solved grows linearly with frequency. Similarly, the three papers mentioned above use a FD, collocation, and FE method, respectively, to solve the P–SV and SH equations. In order to solve these equations, each method requires a number of mesh points in depth (and hence computational effort) that grows linearly with frequency. Finally, the number of time steps needed or the number of frequencies for which the P–SV and SH solutions must be solved grows linearly with $f_{\max}$.

While a cylindrical coordinate system is the natural one for point seismic sources in a laterally homogeneous medium, we shall see later that a Cartesian coordinate system offers certain advantages when extended seismic sources are considered. For that reason, let us consider how this same physical problem can be handled in Cartesian coordinates.

We start by expanding the displacement and z component of stress in terms of an orthogonal set of basis functions

$$\mathbf{u}(x, y, z, \omega) = \int_{-\infty}^{\infty}\int_{-\infty}^{\infty} (U^c\mathbf{R}^c + V^c\mathbf{S}^c + W^c\mathbf{T}^c)\, dk_x\, dk_y, \tag{28}$$

with an equation analogous to Eq. (20) for σ_z, where

$$\mathbf{R}^c = Y\hat{\mathbf{z}}, \tag{29a}$$

$$\mathbf{S}^c = k_x^{-1}\hat{\mathbf{x}}\,\partial_x Y + k_y^{-1}\hat{\mathbf{y}}\,\partial_y Y, \tag{29b}$$

$$\mathbf{T}^c = k_y^{-1}\hat{\mathbf{x}}\,\partial_y Y - k_x^{-1}\hat{\mathbf{y}}\,\partial_x Y, \tag{29c}$$

$$Y(x, y) = \exp(-ik_x x - ik_y y), \tag{30}$$

where U^c, V^c, and W^c are functions of z, k_x, k_y, and ω. One possible route to follow to obtain a solution for $U^c, \ldots, T^c$ would be to use the equations of motion to obtain an equation analogous to Eq. (21) involving the new expansion coefficients, i.e., let

$$\mathbf{b}^c = [U^c, V^c, W^c, P^c, S^c, T^c]^T, \tag{31}$$

$$d_z\mathbf{b}^c = A^c\mathbf{b}^c + \mathbf{F}. \tag{32}$$

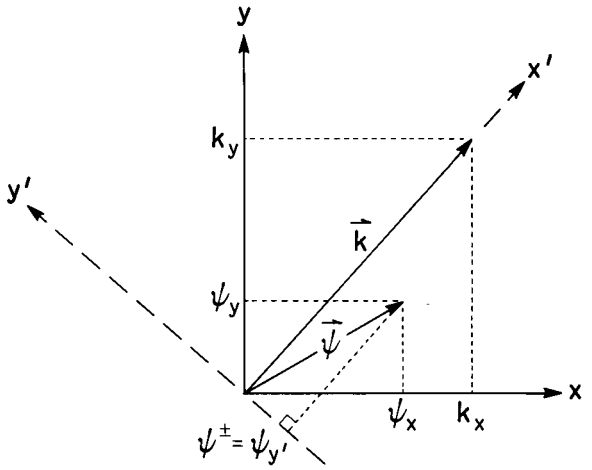

FIG. 3. A plane wave with wave number **k** propagates in the x' direction; **k** lies in the x–y plane. The vector potential Ψ does not necessarily lie in the x–y plane; $\Psi^{\pm}$ is the y' component of Ψ.

However, because the P–SV and SH motions do not separate in a Cartesian coordinate system, A^c is a 6×6 matrix that does not partition into a 4×4 P–SV and a 2×2 SH system like Eqs. (21) and (22). The 6×6 system [Eq. (32)] would have to be solved for every (k_x, k_y) pair.

This problem may be reduced to a problem in which P–SV and SH separate by exploitation of the cylindrical symmetry. For every point (k_x, k_y) in the wave number plane, we choose a new coordinate system (x', y', z) with x' oriented along the direction of the wave number vector $\mathbf{k} = k_x\hat{\mathbf{x}} + k_y\hat{\mathbf{y}}$ (Fig. 3). If we then let $k = |\mathbf{k}|$, and replace U, V, W, P, S, and T in Eqs. (23) and (24) by iu_z, $u_{x'}$, $u_{y'}$, $i\sigma_{zz}$, $\sigma_{x'z}$, and $\sigma_{y'z}$, respectively, we find that Eqs. (21) and (22) hold in the rotated Cartesian system (Kennett, 1983, p. 36). They are then solved for every (k_x, k_y) point yielding radial, transverse, and vertical displacements, and these results are rerotated back into the (x, y, z) system for subsequent use. This technique has been used by Bouchon (1979) and Chouet (1982) for extended sources in layered media.

c. Weakly Inhomogeneous Layers. Thus far, we have restricted our comments to methods of solving the P–SV and SH equations for arbitrary variation of velocity with depth. To accommodate the generality of arbitrary variation, purely numerical methods (e.g., FE, FD, collocation) must be used to solve the equations. If the restrictions on the velocity profile are tightened to require piecewise-continuous functions with small velocity

gradients $d_z\alpha$ and $d_z\beta$ between discontinuities (α being the P-wave velocity and β being the S-wave velocity), then two benefits accrue from the standpoint of extended-source calculations. First, the variations of the Green's functions with depth [i.e., the terms U, V, W, etc., in Eq. (19)] can be written in terms of analytic functions such as Airy functions. Second, the computation times scale like $f_{\max}^2$ rather than $f_{\max}^3$, because the effort of solving the P–SV and SH equations, becomes independent of frequency. Because extended-source calculations have not been done with Green's function methods using the approximation of weakly inhomogeneous layers, we will not dwell on these methods. Cormier (1980), Kennett and Illingworth (1981), and Chapman and Orcutt (1985) describe useful techniques and their antecedents.

d. Uniform Layers. The theory for calculating synthetic seismograms is most fully understood for laterally homogeneous structures in which the material properties are assumed to be piecewise-constant functions of depth, i.e., uniform plane layers bounded by discontinuities. Historically, generalized ray theory has been widely used for calculating synthetic seismograms in layered media for both point dislocations (Helmberger and Malone, 1975; Helmberger and Harkrider, 1978; Liu and Helmberger, 1985) and for extended sources (Hartzell *et al.*, 1978; Heaton and Helmberger, 1979; Archuleta and Hartzell, 1981). Generalized ray theory does not yield complete synthetic seismograms for an inhomogeneous medium. Consequently, it can be safely used for velocity structures having only a few layers, but presents difficulties when used in complicated multilayered earth structures (Hartzell and Helmberger, 1982). For this reason, considerable effort has gone into developing theory for calculating complete synthetic seismograms in layered models. Chin *et al.* (1984a,b) review a number of the methods.

For the purpose of extended source calculations, the assumption of uniform layers has two relevant consequences. First, the expansion coefficients $U(z), V(z), \ldots, T(z)$ in Eqs. (19) and (20) can be expressed as linear combinations of simple exponential functions, rather than as more complicated Airy functions or functions obtained numerically on a grid of points in depth. Second, although not computationally inexpensive, it is at least feasible to calculate these Green's functions up to high frequencies, e.g., 25 Hz.

To elaborate on the first point above, we follow Kennett (1983, pp. 46–48). Within a uniform layer, the displacement-stress vector $\mathbf{b}_P$ from Eq. (21) can be related to the vector $\mathbf{v}$ of upgoing and downgoing P and S potentials through the D_P matrix given by Kennett (1983, p. 48) as

$$\mathbf{b}_P = D_P \mathbf{v}_P, \tag{33}$$

where

$$\mathbf{v}_P(z) = Q_P(z, z_0)\mathbf{v}_P(z_0), \tag{34}$$

$$Q_P(z, z_0) = \text{diag}\{\exp[-i\omega q_\alpha(z - z_0)], \exp[-i\omega q_\beta(z - z_0)], \exp[i\omega q_\alpha(z - z_0)], \exp[i\omega q_\beta(z - z_0)]\}. \tag{35}$$

Here, q_α and q_β are vertical slownesses:

$$q_\alpha = (\alpha^{-2} - p^2)^{1/2}, \tag{36a}$$

$$q_\beta = (\beta^{-2} - p^2)^{1/2}, \tag{36b}$$

$$p = k/\omega. \tag{37}$$

For the SH problem, exactly analogous equations hold, with

$$Q_H(z, z_0) = \text{diag}\{\exp[-i\omega q_\beta(z - z_0)], \exp[i\omega q_\beta(z - z_0)]\}. \tag{38}$$

From the form of Q_P and from Eq. (34), we can see that if we know $\mathbf{v}$ at level z_0, which might be the top of a layer, we can determine $\mathbf{v}$ anywhere within the layer by applying Q_P. Moreover, the phase advance given by the four terms in Q_P corresponds to upgoing P and S waves and downgoing P and S waves, respectively. Hence, the elements of $\mathbf{v}_P$ can be identified as upgoing and downgoing P and SV potentials, as

$$\mathbf{v}_P = [\Phi^+, \Psi^+, \Phi^-, \Psi^-]^T. \tag{39}$$

The matrices $\mathbf{D}_P$ and $\mathbf{D}_H$ are independent of depth within a layer. Since we can obtain $\mathbf{v}$ anywhere within a layer from knowledge of its value on a boundary, we can use $\mathbf{D}$ to obtain $\mathbf{b}$ anywhere within a layer. This is expressed by the construction of the propagator matrix for a uniform layer:

$$P(z, z_0) = D(z)Q(z, z_0)D^{-1}(z_0). \tag{40}$$

Because of the form of Q, Eqs. (35) and (38), $\mathbf{b}$ will be linear combinations of terms containing $\exp[i\omega q(z - z_0)]$. The task of finding $\mathbf{b}$ at each of the interfaces involves solving the P–SV and SH systems at each of the interfaces and is discussed in many of the papers already cited.

The simple exponential forms of the $\mathbf{v}$ and $\mathbf{b}$ vectors can be exploited in two ways for extended source calculations. The first way has been used by Bouchon and Aki (1977) and Bouchon (1979). When an extended seismic source is contained entirely within a layer, the upgoing and downgoing P and S potentials can be calculated directly for the source thanks to the simple form of Q_P, Eq. (35). These upgoing and downgoing source potentials are then used as a source term in the remainder of the synthetic seismogram calculation (this will be elaborated on in Section II.C.A.) The second way of exploiting the simple form of $\mathbf{v}$ and $\mathbf{b}$ has not yet been used.

In order to use the form of the representation theorem Eq. (15), the tractions at all depths must be derived for surface point sources. Equations (33)–(35) show how the tractions within a layer can be written analytically. For certain forms of the slip vector **s**, it may be possible to perform the vertical part of the fault surface integration analytically.

Computational effort usually goes like $f_{\max}^2$ or $f_{\max}$ (depending on the wave number integrations method) for methods using uniform layers. This compares to factors of $f_{\max}^3$ for methods that allow arbitrary variation of material properties with depth. The primary reason for the factor of $f_{\max}$ difference is that the number of layers remains fixed for all frequencies in uniform layer calculations, whereas the number of grid points in depth increases with frequency in methods such as the discrete wave number finite element (DWFE) method (Olson *et al.*, 1984).

More specifically, the calculation time C required by uniform layer methods generally scales like

$$C \approx n_f n_k n_s n_r n_l,$$

where n_f and n_k are the numbers of frequencies and wave numbers (or slownesses) at which Eqs. (21) and (22) are to be solved, n_s and n_r are the number of source and receiver depths desired, and n_l is the number of layers. Here, n_f is clearly a linear function of $f_{\max}$, and n_s, n_r, and n_l are usually fixed for all frequencies. In some methods, such as Kennett (1980), Apsel and Luco (1983), and Yao and Harkrider (1983), it is very easy to place a source or receiver at an interface between layers, in which case

$$C \approx n_f n_k n_s n_l \quad \text{or} \quad n_f n_k n_r n_l,$$

where n_k depends on the method used to do the inverse transform Eq. (19). Kind (1979) and Kennett (1980) use a trapezoidal rule in slowness, so for them n_k is independent of frequency. Apsel and Luco (1983) and Frazer and Gettrust (1984) use a Filon's method in which n_k probably grows roughly linearly with frequency. Bouchon (1981) and Yao and Harkrider (1983) use a discrete wave number summation in which n_k is, in principle, independent of frequency but in practice is linear with frequency due to the convergence criterion used in the wave number integral. Because the functions $U, V, \ldots, T$ in Eqs. (19) and (20) become progressively more oscillatory functions of slowness as frequency increases (see, e.g., Figs. 6 and 7 of Spudich and Ascher, 1983), methods that use a fixed set of slowness points for all frequencies are likely to become inaccurate at sufficiently high frequencies.

A final note is appropriate regarding the "accuracy" of uniform layer Green's function methods when used to generate the seismic response of velocity structures having smooth gradients of velocity with depth. A

uniform layer method will approximate a gradient with a stairstep velocity structure. At sufficiently high frequencies, the seismic wavelengths will shrink to a fraction of the layer thicknesses. The resulting Green's functions will then display considerable reverberative high frequency energy, corresponding to interlayer multiples, which looks gratifyingly like scattered waves in real seismograms. Methods like DWFE (Olson *et al.*, 1984) that are meant to handle gradient zones properly will yield high-frequency Green's functions having simple pulses and lacking all the interlayer multiples. In a certain sense, methods like DWFE can be thought of as using progressively thinner layers to achieve progressively better approximations of a velocity gradient as frequency increases. The DWFE result is the more accurate result for the desired gradient structure. However, it is unclear which Green's function method is better to use considering the scattering caused by lateral heterogeneities in the earth, which neither method can handle.

C. Integrating over the Fault Surface

In this section we discuss how the integrals, Eqs. (12) and (15), have been performed by various investigators. Instead of presenting all of the relevant equations in complete detail, we choose to emphasize the concepts behind the methods. For explicit and implicit Green's function integration methods, the relevant concepts can largely be illustrated with a very simple line-source model of a rupturing fault. For non-Green's function methods, it will be necessary to abandon the line-source problem.

In our simplified problem, the analogs to Eqs. (12) and (15) are

$$u(t) = \int_{-\infty}^{\infty} dt' \int_0^L s(x, t') T(x, t - t')\, dx \tag{41}$$

$$u(\omega) = \int_0^L s(x, \omega) T(x, \omega)\, dx, \tag{42}$$

where s and T are the slip and traction functions on the line source, which extends from $x = 0$ to $x = L$. For some choices of slip and traction, their space and time dependence are separable. Thus, under this assumption the slip function may be written

$$s(x, t) = a_s(x) f_s[t - t_s(x)] = a_s(x) f_s(t) * \delta[t - t_s(x)], \tag{43}$$

where x is a position along the line, a_s is the slip amplitude, $t_s(x)$ is the initiation time of the slip at x, $f_s(t)$ is its time dependence, and the asterisk ($*$) indicates convolution. Similarly, the traction Green's function impinging upon the line may be given by

$$T(x, t) = a_T(x) f_T[t - t_T(x)] = a_T(x) f_T(t) * \delta[t - t_T(x)]. \tag{44}$$

Their temporal Fourier transforms are

$$s(x, \omega) = a_s(x) f_s(\omega) \exp[-i\omega t_s(x)], \tag{45}$$

$$T(x, \omega) = a_T(x) f_T(\omega) \exp[-i\omega t_T(x)]. \tag{46}$$

In the ensuing discussions, we will occasionally simplify further as necessary by assuming that $a_s(x) = a_T(x) = 1$ and $f_s(\omega) = f_T(\omega) = 1$. In particular, we may assume that the traction Green's function is a plane wave, in which case

$$t_T(x) = p_T x, \tag{47}$$

where p_T is the component of the wave's slowness (1/velocity) along the x axis, and we may assume that the source's propagation velocity v_r (rupture velocity) is constant, so that

$$t_s(x) = x/v_r = p_r x, \tag{48}$$

where p_r is rupture slowness (Fig. 5).

1. Ray Theory and Kinematic Sources

Both ray theory and Gaussian beam Green's functions can be calculated rapidly for laterally varying media. Bernard and Madariaga (1984) and Spudich and Frazer (1984) have combined ray theory Green's functions with extended source models, while Červený *et al.* (1987) and Cormier and Beroza (1987) have used Gaussian beams. For simplicity we will demonstrate how ray theory is used with extended sources. A slip function in the form of Eq. (43) is used in many kinematic source models (Section I.A). A Green's function given by Eq. (44) is appropriate for describing a propagating nondispersive pulse, such as the far-field term of the asymptotic ray theory Green's function. In this case $t_T(x)$ is simply the ray theory travel time from x to the observer. Straightforward substitution of these two expressions into the representation theorem, Eq. (41), leads to an exact and rather simple integration formula,

$$u(t) = f_s(t) * f_T(t) * \int_0^L a_s(x) a_T(x) \delta[t - t_a(x)]\, dx, \tag{49}$$

where

$$t_a(x) = t_s(x) + t_T(x) \tag{50}$$

is the arrival time function, i.e., it is the time that a ray generated by the rupturing of x arrives at the observer. Note that the integrand of Eq. (49) is nonzero only where the argument of the delta function is zero, i.e., only for the roots of the equation

$$t - t_a(x) = 0, \quad 0 \le x \le L. \tag{51}$$

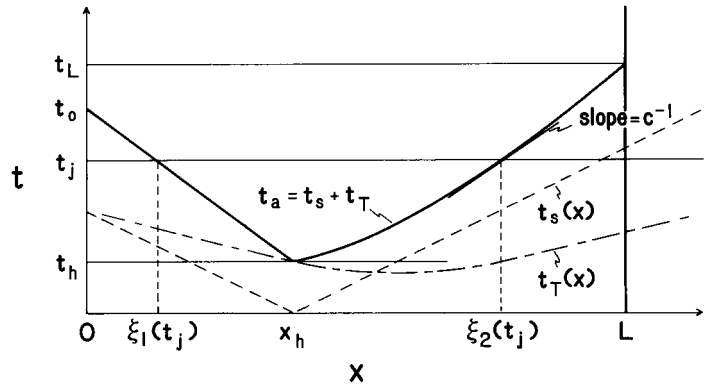

FIG. 4. The rupture time function $t_s(x)$ and the travel time function $t_T(x)$ are added to form the arrival time function t_a. For time $t = t_j$, Eq. (51) has two roots in $[0, L]$, $\xi_1(t_j)$ and $\xi_2(t_j)$.

Hence, the integral Eq. (49) may be converted to a sum over the roots of Eq. (51). The number $m(t)$ of roots in the interval $[0, L]$ will depend on t and on the shapes of the t_s and t_T curves (Fig. 4). Let us denote the roots by $\xi_i(t)$, $i = 1, 2, \ldots, m(t)$. Generally, there will be only one root for unilateral rupture propagation or two roots for bilateral propagation, unless the rupture velocity exceeds the P- or S-wave speed somewhere in $[0, L]$, in which case there may be extra roots. Using the relation

$$\int_{-\infty}^{\infty} a(x)\delta[t - g(x)]\,dx = [a(x)|\partial_x g|^{-1}]|_{t-g(x)=0}, \tag{52}$$

Eq. (49) becomes

$$u(t) = f_s(t) * f_T(t) * \sum_{j=1}^{m(t)} a_s[\xi_j(t)]a_T[\xi_j(t)]c[\xi_j(t)], \tag{53}$$

where

$$c[\xi_j(t)] = |d_t[\xi_j(t)]|. \tag{54}$$

The term c is the velocity of the roots (Fig. 4), and c^{-1} is exactly equal to the seismic directivity function for this line-source problem (Spudich and Frazer, 1984).

Bernard and Madariaga (1984) have introduced the idea of "critical points" to approximate Eq. (53) even further. Consider the behavior of $u(t)$ as t increases from 0 to ∞. For $t < t_h$ (Fig. 4), $m(t) = 0$ and $u(t) = 0$. When t exceeds t_h, $m(t)$ instantaneously jumps to 2 and $u(t)$ instantaneously takes on a finite value. As t approaches t_0, the root $\xi_1(t)$ ap-

proaches 0. When t exceeds t_0, $m(t)$ suddenly drops to 1 and $u(t)$ suffers another jump discontinuity. A similar set of phenomena occurs when t exceeds t_L. Because the high-frequency part of $u(t)$ is dominated by its jump discontinuities, $u(t)$ can be approximated by pulses from the three places on the fault, $x = 0$, x_h, and L, associated with the discontinuities. These are the critical points. In our one-dimensional example, the critical points are the places where roots ξ_1 and ξ_2 either materialize or disappear. An additional critical point can occur at places where c becomes singular, which will happen in the case of super-shear rupture velocity. We note in passing that seismogram amplitudes are linearly related to c, which is a nonlinear function of rupture time. This explains the strong influence of rupture time variation on seismogram amplitudes noted by Archuleta (1984).

For a two-dimensional fault, the result of Eq. (53) is easily generalized. If $\mathbf{x}$ is a position on the fault surface Σ, then the arrival time function is

$$t_a(\mathbf{x}) = t_s(\mathbf{x}) + t_T(\mathbf{x}). \tag{55}$$

The equation

$$t - t_a(\mathbf{x}) = 0 \tag{56}$$

is satisfied on the curve $\xi(t)$, which is an equal time contour [called an isochrone by Bernard and Madariaga (1984)] of the t_a function. The term c now becomes the velocity of an isochrone perpendicular to its length

$$c(\mathbf{x}) = |\nabla t_a(\mathbf{x})|^{-1}, \tag{57}$$

and the two-dimensional analog of Eq. (53) is

$$u(t) = f_s(t) * f_T(t) * I(t), \tag{58a}$$

$$I(t) = \int_{\xi(t)} a_s(\mathbf{x}) a_T(\mathbf{x}) c(\mathbf{x})\, dl, \tag{58b}$$

where l is the arc length along the curve $\xi(t)$. Each time point in the seismogram is obtained by doing a line integral along an isochrone. Evaluation of $I(t)$ in Eq. (58b) is quite simple for an arbitrarily complicated $t_a(\mathbf{x})$ using the algorithm of Spudich and Frazer (1984). A large fault Σ is broken into a set of triangular subfaults. If the three vertices of a triangle are located at $\mathbf{x}_1$, $\mathbf{x}_2$, and $\mathbf{x}_3$, we define the quantities

$$g_i = a_s(\mathbf{x}_i) a_T(\mathbf{x}_i), \tag{59}$$

$$\tau_i = t_a(\mathbf{x}_i) \tag{60}$$

for $i = 1, 2, 3$, and we approximate g and τ for $\mathbf{x}$ inside the triangle by linear interpolation between the values at the three vertices. Then $c(\mathbf{x})$ is constant within a triangle, isochrones are easily found straight lines cutting across the triangle, and the integrand $g(\mathbf{x})$ is a linear function along an

isochrone and can be integrated exactly. Using this approach $I(t)$ is obtained separately for each triangular subfault; the subfaults may be dealt with in any sequence, and no complicated curve-following algorithm is needed to integrate along the isochrones. A typical calculation may involve 5000 subfaults.

Note that the result expressed in Eqs. (58a and b) is the exact result for the far-field Green's functions and is valid even when the observer is very close to the source. Spudich and Frazer (1984) note that the term "far-field" has been used both to describe certain terms in the Green's function and to describe a region, far from an extended seismic source, where the Fraunhofer approximation holds (Aki and Richards, 1980, pp. 804–805). They suggest the use of the terms far-source and near-source to describe the region where the Fraunhofer approximation is valid or invalid, respectively. Thus, Eqs. (58a and b) are the results valid in the near-source region for far-field Green's functions. What is missing from Eqs. (58a and b) is the near-field term of the Green's function. Because the near-field term is inherently lower in frequency than the far-field term, and because it decays more rapidly with distance, omission of this term leads to low-frequency errors at short epicentral distances. Farra *et al.* (1986) have investigated the importance of this omission. They have additionally extended the isochrone-integration technique to include multiple rays and maximum time pulses.

2. Point Source Summation

In performing the integrals Eqs. (12) and (15), an assumption frequently made in seismology is that a large earthquake can be simulated by a grid of point dislocations (Heaton and Helmberger, 1979; Archuleta and Hartzell, 1981; Bouchon, 1982; Heaton, 1982; Hartzell and Helmberger, 1982; Campillo and Bouchon, 1983; Liu and Helmberger, 1983). In this case the integrals over the fault surface in Eqs. (12) and (15) are replaced by a summation of all the point sources, i.e., Eq. (41) is approximated by

$$u(t) \approx \sum_{j=1}^{n} s(x_j, t) * T(x_j, t)\, \Delta x_j, \tag{61}$$

and Eq. (42) is approximated by

$$u(\omega) \approx \sum_{j=1}^{n} s(x_j, \omega) T(x_j, \omega)\, \Delta x_j, \tag{62}$$

where the interval $[0, L]$ has been broken into n segments of width Δx_j with sample point x_j at the midpoint of segment j. Both Eqs. (61) and (62) are straightforward to compute and should yield identical results. For this

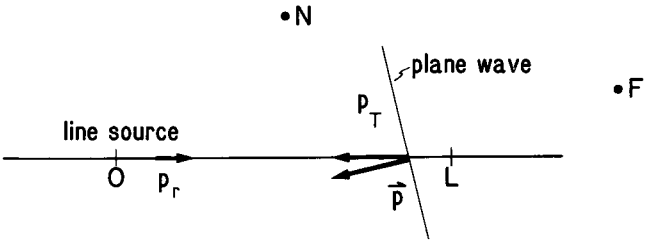

FIG. 5. A seismic source propagates from $x = 0$ to $x = L$ with slowness p_r. Plane waves emitted from distant observers at **B**, **N**, and **F** propagate with true slowness **p**, and the component of wave slowness along the x axis is p_T.

reason we will refer to the point-source summation technique without always being specific about whether it is performed in the time or frequency domain.

The accuracy of the technique is more easily understood by analyzing the frequency-domain version. The point-source summation technique evaluates Eq. (62) by using the familiar midpoint rule for numerical quadrature. The accuracy of this approximation is highly dependent upon frequency and upon the observer's position with respect to the rupture propagation direction, as can be easily shown in our simple example. For simplicity, assume a plane wave, Eq. (47), and a constant rupture velocity, Eq. (48), and ignore amplitude variations and source time functions. Then

$$sT = \exp[-i\omega(p_r + p_T)x]. \tag{63}$$

If we are considering S waves from the rupture, and if the rupture velocity is close to the shear velocity, then from Fig. 5 it is clear that $p_r + p_T \approx 0$ for observers in the forward direction; $p_r + p_T \approx p_r$ for observers normal to the fault; $p_r + p_T \approx 2p_r$ for observers in the backward direction. In Fig. 6 it can be seen that the integrand becomes progressively more oscillatory as frequency increases or as the observer moves toward B. If the sample points $\{x_j\}$ in Eq. (62) are held fixed for all frequencies and observers, the computed value of $u(\omega)$ will be more accurate for low frequencies than high and for observers in the forward direction. In fact, this breakdown of the point-source approximation is well known (Hartzell *et al.*, 1978), and examples will be shown in Section III.A.1.

If evaluation of the integrand were easy, the most straightforward way to improve accuracy would be to decrease the sample spacing Δx_j until the integral converged to a stable value. However, for dynamic source models, $s(x, t)$ can be very expensive to calculate, as can $T(x, t)$ for complete Green's functions. Hence, in general, we would like to perform Eq. (42) with as few expensive integrand evaluations as possible.

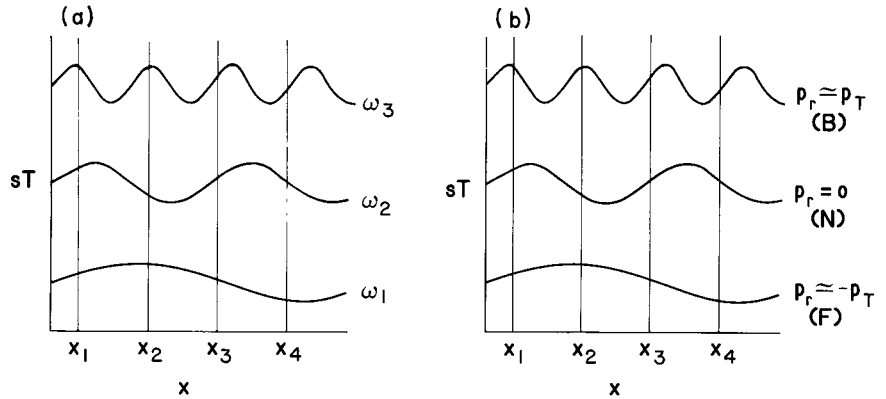

FIG. 6. Behavior of sT as a function of position. (a) $p_r + p_T$ is held fixed and sT is plotted for three differing frequencies (with vertical offsets). (b) The frequency ω is held fixed and sT is plotted for observers in the direction of rupture (**F**), normal to the fault (**N**) and opposite the direction of rupture (**B**). See also Fig. 5. Here $x_1, \ldots, x_4$ are sample points for the numerical quadrature. Clearly the integrand becomes undersampled as ω becomes large and when $p_r + p_T$ becomes large.

3. Improvements on Point Source Summation Using Kinematic Slip Functions and Complete Green's Functions

Let us consider how the quadrature Eq. (62) can be improved under the assumptions that s is easily calculated and T is quite expensive to calculate. This case corresponds to the most commonly employed approximations used in actual ground motion modeling: s is derived from a kinematic source model, while T is a complete Green's function.

Under these assumptions, the basic approach has been to make the sample intervals $\{\Delta x_j\}$ as small as necessary to ensure convergence of the sum Eq. (62). Because the calculation of s is easy, it is obtained exactly at each sample point. However, T is calculated exactly only at a few widely spaced sample points, and it is derived at the intervening quadrature points $\{x_j\}$ by an interpolation scheme.

a. Explicit Interpolation of Green's Functions in the Frequency Domain. The method of Spudich (1981), which was used by Archuleta (1984) to model the 1979 Imperial Valley earthquake, interpolates T explicitly in the frequency domain and works as follows. From Eqs. (45)–(48) we can see that s and T are basically oscillatory functions of position with spatial wavelengths v_r/f for s and β/f for T, where f is the frequency $\omega/2\pi$ and β is the shear wave velocity. Because generally $v_r < \beta$, the spatial wavelength of s is less than that of T for equivalent f. Then, T may be specified

by exact calculation of its values on a grid of points $\{x_{T_j}\}$ with spacing

$$\Delta x_T(x, f) = \beta(x)/(mf), \tag{64}$$

where m is the desired number of sample points per shear wavelength. Similarly, s is specified by exact calculation on a grid of points $\{x_{s_j}\}$ with spacing

$$\Delta x_s(x, f) = v_r(x)/(nf), \tag{65}$$

where n is a desired number of sample points. Note that the sample spacing decreases as frequency increases (Fig. 6), and that it can also vary depending on local S-wave and rupture velocities. In addition n can be chosen larger than m to improve accuracy. Consequently, the method of Spudich (1981) can be regarded as a crudely adaptive quadrature with the adaptive rules built in *a priori*. Equations (64) and (65) cannot be used for very low frequencies because s and T are not constant over the fault at $\omega = 0$. In practice some maximum allowable Δx_s and Δx_T are specified and used when Eqs. (64) and (65) specify greater Δx_s and Δx_T.

Trapezoidal-rule quadrature of the product sT is performed separately for each frequency, with the quadrature points being the sample points $\{x_{s_j}\}$ of s, and with the values of T at the points $\{x_{s_j}\}$ derived from the exact values at $\{x_{T_j}\}$ by linear interpolation (Fig. 7). Two strengths of this procedure are that the error of the quadrature is independent of frequency (unlike direct point-source summation) and that the method for interpolating T is valid regardless of the types of seismic waves that comprise T. The

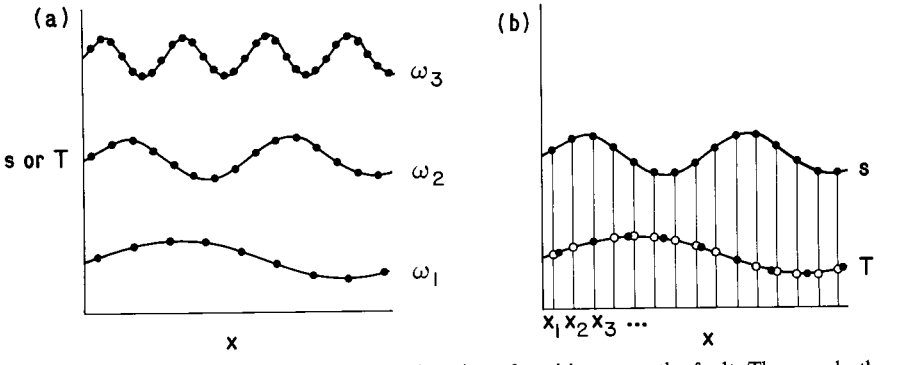

FIG. 7. (a) Both s and T oscillate as a function of position x on the fault. They are both evaluated exactly at sample points whose spacing decreases with increasing frequency. (b) Here, s and T do not have the same wavelength on the fault; s is evaluated exactly at quadrature points $x_1, x_2, \ldots$, while values of T at the quadrature points are determined by linear interpolation between nearby exact values. The closed circle (●) indicates values calculated exactly and the open circle (○) indicates values derived by linear interpolation.

method's chief disadvantages are that computational effort and storage are proportional to the cube of the frequency bandwidth for two-dimensional faults. For any single frequency f, the number of quadrature points on the fault is proportional to $(\Delta x_T)^{-2}$ or f^2. Hence, to obtain seismograms in the frequency band $(0, f_{\max})$, computing effort and Green's function storage scale like $f_{\max}^3$. This scaling limits the frequency band in which the adaptive method may be applied. We note in passing that we have also tried to integrate sT by Gaussian quadrature and by analytic integration of a piecewise cubic spline passed through the samples of sT, but have found the trapezoidal rule to be more dependable. While it is true that other integration methods converge more quickly than trapezoidal rule as sample spacing decreases, the obverse of that statement is also true; other methods diverge more rapidly as sample spacing increases. Our experience is that trapezoidal rule gives the most reliable results in massive computations that operate on the verge of undersampling. However, we have not investigated other quadrature methods exhaustively.

b. Explicit Interpolation of Green's Functions in the Time Domain. At present there are time-domain Green's function interpolation methods that avoid the $f_{\max}^3$ storage requirement for Green's functions at the expense of a less accurate interpolation scheme. Some investigators (see, e.g., Hartzell *et al.*, 1978; Heaton and Helmberger, 1979; Heaton, 1982; Hartzell and Helmberger, 1982; Liu and Helmberger, 1983) perform an explicit time-domain point-source summation of the form

$$u(t) = \int_0^L a_s(x) f_s(t) * \delta[t - t_s(x)] * T(x, t)\, dx, \tag{66}$$

$$u(t) = f_s(t) * \int_0^L a_s(x) T[x, t - t_s(x)]\, dx$$

$$\approx f_s(t) * \sum_{j=1}^{n} a_s(x_j) T[x_j, t - t_s(x_j)]\, \Delta x_j, \tag{67}$$

where Eq. (43) has been used to define $s(x, t)$ but $T(x, t)$ has been left general. Because the slip time function f_s is independent of position, it has been factored out of the sum. Because T is expensive to calculate, it is obtained on a sparse grid of points $\{x_{T_j}\}$ and its value at quadrature points x_j is obtained by linear interpolation that incorporates a particular physical assumption about T. Hartzell *et al.* (1978) assume that T is composed of a set of dispersive pulses that can be separated in time and have characteristic phase velocities. In their method each pulse in a seismogram is interpolated individually. For a half-space there are only four pulses, P, S, SP, and the Rayleigh wave. Suppose that exact Green's functions are known at x_{T_i} and

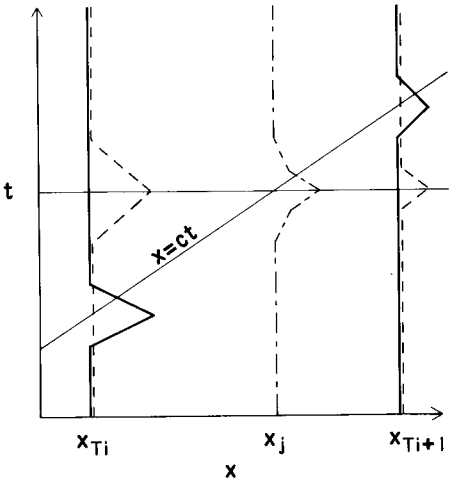

FIG. 8. Exact Green's functions calculated at x_{T_i} and $x_{T_{i+1}}$. Each contain a pulse traveling at velocity c. Exact seismograms are appropriately stretched or compressed so that the pulses align horizontally. Linear interpolation can then be done to obtain a Green's function at x_j (——, exact; – – –, stretched; —·—, interpolated).

$x_{T_{i+1}}$, and we desire to interpolate between these two points to obtain an approximate Green's function at x_j. Suppose also that we interpolate a single pulse that arrives at x_{T_i} at time t_i and at x_j at time t_j. Then the interpolation rule of Hartzell *et al.* (1978) is

$$T(x_j, t) = \frac{t_i}{t_j}\left|\frac{t_j - t_{i+1}}{t_i - t_{i+1}}\right| T\left[x_{T_i}, \frac{t_i}{t_j}t\right] + \frac{t_{i+1}}{t_j}\left|\frac{t_i - t_j}{t_i - t_{i+1}}\right| T\left[x_{T_{i+1}}, \left(\frac{t_{i+1}}{t_j}\right)t\right]. \tag{68}$$

The exact Green's functions are first stretched or compressed in the time domain. They are weighted by a factor that introduces a R^{-1} amplitude behavior in addition to the usual linear interpolation weighting factor (Fig. 8). This procedure works very well for a half-space (Fig. 9) but introduces pulse shape distortions for nondispersive waves (Fig. 8).

In many cases the largest pulse in a Green's function is a body wave similar to the direct S wave, in which case the time stretching used by Hartzell *et al.* (1978) can be replaced by a simple time shift that aligns the important pulse (Heaton and Helmberger, 1979; Heaton, 1982; and Hartzell and Helmberger, 1982). In this technique the R^{-1} scaling is also

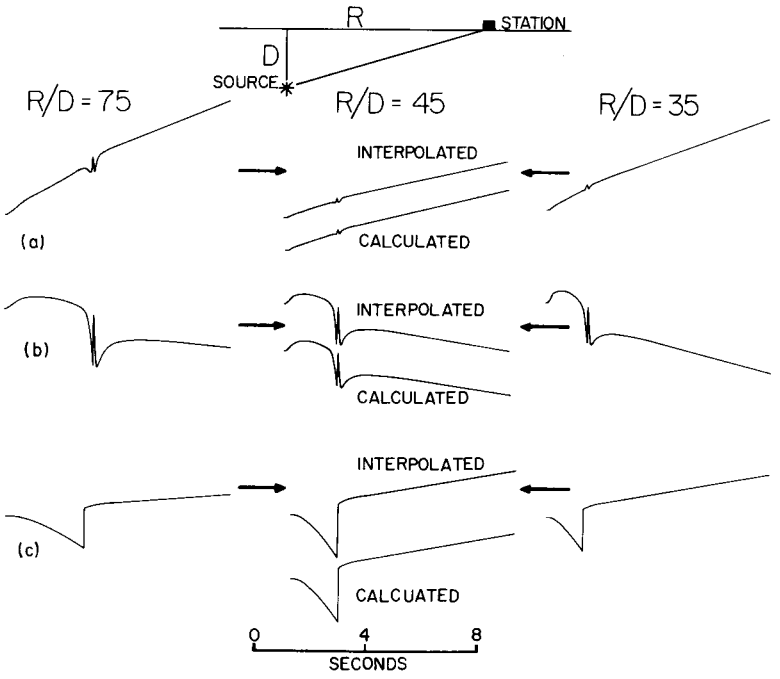

FIG. 9. Examples of linearly interpolated Green's functions for (a) radial (R), (b) vertical (z), and (c) azimuthal (ϕ) components of displacement for a strike-slip double-couple source, from Hartzell *et al.* (1978). The interpolated Green's functions are compared with those calculated directly by a Cagniard–deHoop method. (Reprinted with permission from the *Bulletin of the Seismological Society of America*.)

omitted, in which case Eq. (68) becomes

$$T(x_j, t) = \left|\frac{t_j - t_{i+1}}{t_i - t_{i+1}}\right| T(x_{T_i}, t + t_i - t_j) + \left|\frac{t_{i+1} - t_j}{t_i - t_{i+1}}\right| T(x_{T_{i+1}}, t + t_{i+1} - t_j), \tag{69}$$

which corresponds to shifting the time series the same amount as indicated in Fig. 8 without stretching the seismograms. The implementation of both Eqs. (68) and (69) becomes quite complicated if pulses having differing phase velocities cross, and if the exact Green's functions do not consist of distinct arrivals, the methods break down. In practice, this interpolation is generally used assuming that the S wave is the only significant arrival, which is usually true near buried seismic sources. Interpolation using S-wave phase velocities will cause errors for waves traveling at other

velocities, such as P waves and surface waves. For interpolation when a mixture of waves is present, slant-stacking techniques may prove useful (Cabrera and Levy, 1984). The advantage of the procedures presented in Eqs. (68) and (69) is that for calculations in the frequency band $(0, f_{\max})$, the storage space required for the Green's functions is proportional to $f_{\max}$, which is much more manageable than $f_{\max}^3$. In addition a minimal number of expensive theoretical Green's function evaluations are needed. However, the actual performance of the point-source summation Eq. (61) is not facilitated by this interpolation.

c. Implicit Green's Function Extrapolation Using Temporal Convolution. Using the assumption that the Green's function is dominated by the S wave, Apsel *et al.* (1981) have developed a simple procedure, using isochrone integration, which simultaneously extrapolates the Green's functions and includes the effects of rupture propagation. Suppose we have calculated $T(x, t)$ exactly on a set of sample points $\{x_{T_j}\}$, and we wish to approximate $T(x, t)$ at nearby points simply by shifting $T(x_{T_j}, t)$ forward or backward in time so that the S wave of the interpolated seismogram always arrives at x at time $t_T(x)$, as in Eq. (44). We may also want to modify the amplitude of the interpolated seismogram by some factor $A(x, x_{T_j})$ to account for geometric spreading or other factors. Then our extrapolated Green's function may be written

$$T(x, t) = A(x, x_{T_j})T\big(x_{T_j}, t\big) * \delta\big[t + t_T(x_{T_j}) - t_T(x)\big], \tag{70}$$

with $A(x_{T_j}, x_{T_j}) = 1$. Note that Eq. (70) involves only x_{T_j}. For this reason Eq. (70) is an extrapolation. Let our integration interval $[0, L]$ be broken into n domains of width Δx_{T_j}, $j = 1, 2, \ldots, n$, with each domain covering the interval $[x_{L_j}, x_{G_j}]$. Let the slip be given by

$$s(x, t) = a_s(x) f_s(t) * \delta[t - t_s(x)], \tag{71}$$

where $t_s(x)$ is the time that rupture initiates at point x, and $f_s(t)$ is the slip time function, which in this simple example we fix to be independent of position. From Eq. (41) we then have

$$u(t) \approx f_s(t) * \sum_{j=1}^{n} T\big(x_{T_j}, t\big) * I_j(t), \tag{72}$$

$$I_j(t) = \int_{x_{L_j}}^{x_{G_j}} a_s(x) A(x, x_{T_j}) \delta\big[t - t_{a_j}(x)\big]\, dx, \tag{73}$$

where

$$t_{a_j}(x) = t_T(x) - t_T(x_{T_j}) + t_s(x) \tag{74}$$

is an arrival time function analogous to Eq. (50). Thus, applying the same

trick of Eq. (52) to Eq. (73) gives

$$I_j(t) = \sum_{k=1}^{m(t)} a_s[\xi_k(t)] A\left[\xi_k(t), x_{T_j}\right] c[\xi_k(t)], \tag{75}$$

where $\{\xi_k(t)\}$ are the $m(t)$ roots of $t - t_{a_j}(x) = 0$ in the interval $[x_{L_j}, x_{G_j}]$, and where

$$c[\xi_k(t)] = |d_t \xi_k(t)|. \tag{76}$$

Thus, $I_j(t)$ is a convolution filter that is applied to the point-source Green's function $T(x_{T_j}, t)$ in Eq. (72) to correct it for the effect of rupture propagation across the domain $[x_{L_j}, x_{G_j}]$, using the extrapolation rule of Eq. (70) for Green's functions. As long as the extrapolation rule is valid (i.e., as long as most of the energy in the Green's functions propagates at the S-wave velocity), use of Eqs. (72) and (75) will lead to a synthetic seismogram that is independent of grid size Δx_T. Of course, phases traveling at other velocities, such as surface waves, will not be interpolated properly. For the amplitude correction factor A, Apsel *et al.* (1981) use

$$A(x, x_{T_j}) = \left[r(x_{T_j})/r(x)\right]^P, \tag{77}$$

where $r(x)$ is the distance from the observer to the point x on the fault, and P is approximately 2.0. However, they point out that the amplitude correction is of considerably less importance than the time correction, particularly at distances greater than 5 or 10 km. Equation (72) assumes that the slip function $f_s(t)$ is the same over the entire fault. If the slip time function is independent of position within each domain $[x_{L_j}, x_{G_j}]$ but varies from domain to domain, then Eq. (72) may be rewritten

$$u(t) \approx \sum_{j=1}^{n} f_s\left(x_{T_j}, t\right) * T\left(x_{T_j}, t\right) * I_j(t). \tag{78}$$

If further spatial variability of f_s is desired, then the domain $[x_{L_j}, x_{G_j}]$ can be subdivided into many smaller subdomains in which f_s is position independent, and $I_j(t)$ can be written as a sum of terms, each similar to Eq. (75) and each convolved with its own $f_s(t)$. This would be a computational inexpensive way of allowing $f_s(t)$ to vary within $[x_{L_j}, x_{G_j}]$. Similar to the explicit time-domain Green's function interpolation methods, this implicit extrapolation method requires a relatively small number of exact Green's function evaluations, and the necessary Green's function storage grows linearly with frequency bandwidth. The computational effort of calculating $I_j(t)$ in Eq. (73) and its two-dimensional analog Eq. (58b) probably scales like $f_{\max}^2$ for a two-dimensional fault because the necessary time sampling interval goes like $f_{\max}^{-1}$, as does the length of the line integral segment dl in Eq. (58b).

4. A Non-Green's Function Method Using Simple Kinematic Source Models in a Layered Medium

Thus far all the methods that we have discussed that use complete Green's functions have been explicit Green's function integration methods. In all these methods, the slip models and the Green's function T are calculated independently of each other. Bouchon and Aki (1977) and Bouchon (1979) introduced a non-Green's function method in which an extended seismic source is explicitly used for the source term for wave propagation in a layered medium. This is made easy for them by their use of Cartesian coordinates in a homogeneous layer. In the following discussion we follow the derivation by Chouet (1987). We saw earlier in a laterally homogeneous medium how the effect of a point seismic source at depth can be included as a discontinuity in the displacement-stress vector $\mathbf{b}$ at depth z. When an extended seismic source is enclosed within a uniform layer, the effect of the extended source may be included in a different way by determining the stresses and displacements it causes on the overlying and underlying layer interfaces. Propagator matrices are then used to relate these source-induced stresses and displacements to those at the free surface and in the underlying half-space. Once this is done, the wave propagation through the layers is accomplished using the method of Dunkin (1965). While the use of Cartesian coordinates is not essential to the method, it simplifies the integrals over the sources that are used to determine the stresses and displacements it causes.

We start with a layered velocity structure, as in Fig. 10 and the Cartesian coordinate system of Fig. 3. The ground displacement $\mathbf{u}$ may be written

$$\mathbf{u}(x, y, z, \omega) = \int_{-\infty}^{\infty}\int_{-\infty}^{\infty} \mathbf{u}(k_x, k_y, z, \omega) \exp(-ik_x x - ik_y y)\, dk_x\, dk_y. \tag{79}$$

As discussed in Section II.B.2.b, to obtain $\mathbf{u}(k_x, k_y, z, \omega)$ at a particular point (k_x, k_y) involves the solution of the P–SV and SH problems for a plane wave with wave number $\mathbf{k} = k_x\hat{\mathbf{x}} + k_y\hat{\mathbf{y}}$. This yields radial, transverse, and vertical displacements $u_{x'}$, $u_{y'}$, and u_z, which are all functions of k_x, k_y, z, and ω. Displacements in the x and y directions are obtained by

$$u_x = (k_x/k)u_{x'} - (k_y/k)u_{y'}, \tag{80a}$$

and

$$u_y = (k_y/k)u_{x'} - (k_x/k)u_{y'}, \tag{80b}$$

where $k = |\mathbf{k}|$.

We follow Chouet (1987) in obtaining $u_{x'}$, $u_{y'}$, and u_z for an extended source. Consider first the P–SV problem and define the displacement-stress

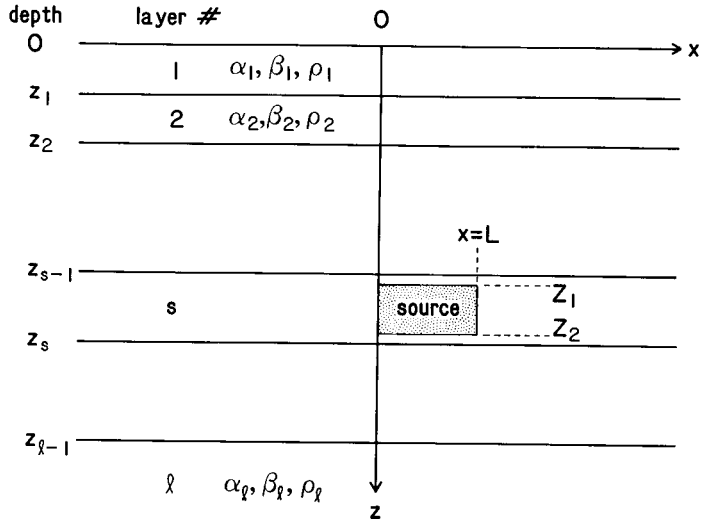

FIG. 10. Cross section of a homogeneously layered earth model. Material properties are constant within each layer. The source is a strike-slip fault in the x–z plane extending from $x = 0$ to $x = L$ and bounded by depths Z_1 and Z_2. Slip is uniform over the fault, and rupture propagates in the $+x$ direction as a vertical line with velocity v_r.

vector $\mathbf{b}$ to be $[u_{x'}, u_z, \sigma_{zz}, \sigma_{zx'}]^T$. We note that this definition is slightly different from Kennett's. Following the layer numbering scheme of Fig. 10, let $\mathbf{b}_n(z)$ be the displacement-stress vector at depth z in layer n. Assume for the moment that we know $\mathbf{b}_s^0(z_{s-1})$ and $\mathbf{b}_s^0(z_s)$, which are the displacement-stress vectors above and below the source caused by upgoing and downgoing waves, respectively, generated by the source. The total displacement-stress vector at depth z_{s-1}, $\mathbf{b}_s(z_{s-1})$, is a sum of the upgoing waves from the source, $\mathbf{b}_s^0(z_{s-1})$, and reverberated waves coming from other depths. We relate $\mathbf{b}$ at the top of the source layer to $\mathbf{b}$ at the free surface:

$$\mathbf{b}_s(z_{s-1}) = P_{s-1}P_{s-2} \cdots P_1\mathbf{b}_1(0), \tag{81}$$

where we define P_n to be the propagator across the nth layer,

$$P_n = P_n(z_{n-1}, z_n). \tag{82}$$

The $\mathbf{b}$ at the bottom of the source layer is related to $\mathbf{b}$ in layer l, the underlying half-space, by

$$\mathbf{b}_l(z_{l-1}) = P_{l-1}P_{l-2} \cdots P_{s+1}\mathbf{b}_{s+1}(z_s) \tag{83}$$

and from Eq. (33)

$$\mathbf{v}_l(z_{l-1}) + D_l^{-1}\mathbf{b}_l(z_{l-1}). \tag{84}$$

Our boundary conditions are a stress-free surface at $z = 0$,

$$\mathbf{b}_1(0) = [u_{x'}, u_z, 0, 0]^T, \tag{85}$$

no upgoing waves in layer l,

$$\mathbf{v}_l(z_{l-1}) = [0, 0, \Phi^-, \Psi^-]^T, \tag{86}$$

and continuity of $\mathbf{b}$ across all interfaces,

$$\mathbf{b}_{i+1}(z_i) = \mathbf{b}_i(z_i), \qquad i = 1, \ldots, s-1, s, \ldots, l-1. \tag{87}$$

We note that Eq. (87) shows explicitly that in Chouet's (1987) formulation the source contribution does not cause a discontinuity in $\mathbf{b}$ at an interface. Then

$$\mathbf{b}_s(z_s) - \mathbf{b}_s^0(z_s) = P_s[\mathbf{b}_s(z_{s-1}) - \mathbf{b}_s^0(z_{s-1})], \tag{88}$$

i.e., the propagator connects only the reverberated components of the waves at levels z_{s-1} and z_s. Skipping the details of the subsequent derivation, which are found in Chouet (1987), we finally obtain

$$\begin{bmatrix} u_{x'}(k_x, k_y) \\ \\ u_z(k_x, k_y) \end{bmatrix} = R_{11}^{-1}[Q_{11}Q_{12}\mathbf{b}_s^0(z_{s-1}) - P_{11}P_{12}\mathbf{b}_s^0(z_s)] \tag{89}$$

for the radial displacement $u_{x'}$ and vertical displacement u_z caused by source terms $\mathbf{b}_s^0(z_{s-1})$ and $\mathbf{b}_s^0(z_s)$. Here,

$$P = D_l^{-1}P_{l-1} \cdots P_{s+1}, \tag{90a}$$

$$Q = P_{l-1} \cdots P_s, \tag{90b}$$

and

$$R = D_{l-1}^{-1}P_{l-1} \cdots P_1, \tag{90c}$$

and each of these 4×4 matrices is partitioned into four 2×2 matrices, e.g.,

$$R = \left[\begin{array}{c|c} R_{11} & R_{12} \\ \hline R_{21} & R_{22} \end{array}\right]. \tag{91}$$

The matrix R_{11}^{-1} may be written

$$R_{11}^{-1} = \tilde{R}_{11}/|R_{11}|, \tag{92}$$

where $|R_{11}|$ is the determinant of R_{11} and is the secular function for the layered medium and $\tilde{R}_{11}$ is the transpose of the cofactor of R_{11}. Of course, direct evaluation of $|R_{11}|$ and products $\tilde{R}_{11}Q_{11}$ and $\tilde{R}_{11}P_{11}$ lead to well-known instabilities (Chin *et al.*, 1984b). Bouchon (1979) and Chouet (1981, 1987) use the method of Dunkin (1965) to evaluate these terms. Equation

(89) is used to obtain $u_{x'}$ and u_z, and $u_{y'}$ is found using a similar equation for the SH problem. Displacements in the x–y–z coordinate system for a plane wave with wave number $\mathbf{k}$ are derived from Eqs. (80a and b), and the total ground motion is a sum of all the plane wave components of Eq. (79). We comment later on how this integral is performed.

We now turn to the derivation of $\mathbf{b}_s^0(z_{s-1})$ and $\mathbf{b}_s(z_s)$, the displacement-stress vectors resulting above and below the source from the upgoing and downgoing source radiation. We follow the approach of Bouchon (1979) and integrate the upgoing and downgoing P and S potentials and then use Eq. (33).

The displacements $\mathbf{u}$ in the medium are related to the potentials Φ and Ψ by

$$\mathbf{u} = \nabla \Phi + \nabla \times \Psi, \qquad \nabla \cdot \Psi = 0, \tag{93}$$

where $\Psi = (\Psi_x, \Psi_y, \Psi_z)^T$ (Fig. 3), and Φ and Ψ are solutions to the wave equations

$$\nabla^2 \Phi = 1/\alpha^2 \, \partial_t^2 \Phi, \tag{94a}$$

$$\nabla^2 \Psi = 1/\beta^2 \, \partial_t^2 \Psi. \tag{94b}$$

Within a uniform layer, they may be written as plane waves of the form

$$\Phi(\omega) = A \exp(-ik_x x - ik_y y \pm i\nu z), \tag{95a}$$

$$\Psi(\omega) = \mathbf{B} \exp(-ik_x x - ik_y y \pm i\gamma z), \tag{95b}$$

where

$$\nu = \left(k_\alpha^2 - k_x^2 - k_y^2\right)^{1/2}, \qquad \operatorname{Im} \nu \le 0, \tag{96a}$$

and

$$\gamma = \left(k_\beta^2 - k_x^2 - k_y^2\right)^{1/2}, \qquad \operatorname{Im} \gamma \le 0, \tag{96b}$$

are vertical wave numbers with $k_\alpha = \omega/\alpha$ and $k_\beta = \omega/\beta$ being wave numbers along the direction of propagation of P and S waves, respectively. The plus and minus signs correspond to upward and downward propagation, respectively.

A point dislocation can be represented by an equivalent double couple of point forces. If Φ^x, Ψ^x; Φ^y, Ψ^y; and Φ^z, Ψ^z are the potentials radiated by point forces applied at (x_0, y_0, z_0) in the x, y, and z directions, respectively, then the potentials radiated by a point dislocation at (x_0, y_0, z_0) having the same mechanism as our extended source (Fig. 10) are

$$\Phi_p(x, y, z) = m(x_0, z_0)\left[\partial_{y_0} \Phi^x(x, y, z) + \partial_{x_0} \Phi^y(x, y, z)\right] \tag{97a}$$

and

$$\Psi_p(x, y, z) = m(x_0, z_0)\left[\partial_{y_0}\Psi^x(x, y, z) + \partial_{x_0}\Psi^y(x, y, z)\right], \quad (97b)$$

where $m(x_0, z_0)$ is the moment density per unit area of the source. Equations (97a and b) are valid for a left-lateral, strike-slip dislocation. Similar terms can be found for other dislocation mechanisms. Hence, to find the total potential radiated by an extended source, we integrate Eqs. (97a and b) over the fault surface. If slip on the fault is given by $s(x_0, z_0, \omega)$, then the radiated compressional potential is

$$\Phi(x, y, z, \omega) = \mu_s \int_{Z_1}^{Z_2} \int_0^L s(x_0, z_0, \omega)[\partial_{y_0}\Phi^x + \partial_{x_0}\Phi^y]\, dx_0\, dz_0, \quad (98)$$

with a similar expression for Ψ. The expressions for the potentials radiated by a point force in the x direction are of the form

$$\Phi^x \approx (k_x/\nu)\exp[-ik_x(x - x_0) - ik_y(y - y_0) - i\nu|z - z_0|], \quad (99a)$$

and

$$\Psi_z^x \approx (k_y/\gamma)\exp[-ik_x(x - x_0) - ik_y(y - y_0) - i\gamma|z - z_0|] \quad (99b)$$

(Bouchon, 1979, Eq. (13)), with similar expressions for other components of Ψ and point-force directions. The absolute value signs in Eqs. (99a and b) ensure that we have downgoing waves below the source depth z_0 and upgoing waves above. For simplicity we define

$$e_p = \exp[-ik_x(x - x_0) - ik_y(y - y_0) - i\nu|z - z_0|] \quad (100a)$$

and

$$e_s = \exp[-ik_x(x - x_0) - ik_y(y - y_0) - i\gamma|z - z_0|]. \quad (100b)$$

Because of the form of the potentials, Eqs. (99a and b), spatial differentiation to obtain the potentials caused by force couples is easy, e.g.,

$$\partial_{x_0}\Phi^x = ik_x\Phi^x. \quad (101)$$

Hence, the compressional potential radiated from the extended source of Eq. (98) will be a sum of terms of the form

$$\Phi(k_x, k_y, z, \omega) \approx F(\omega, k_x, k_y) I_F, \quad (102)$$

where

$$I_F = \int_{Z_1}^{Z_2} \int_0^L \mu s e_p\, dx_0\, dz_0, \quad (103)$$

and where $F(\omega, k_x, k_y)$ is a product of terms like the k_x/ν in Eq. (99a), and the ik_x in Eq. (101). Similar expressions can be written for Ψ. We separate F from the integrated source term I_F to emphasize that I_F is the

two-dimensional Fourier transform of the slip distribution. If the slip function s is sufficiently simple, I_F can be obtained analytically. For example, Bouchon (1979) accomplishes this by using

$$s(x_0, z_0, \omega) = (D/i\omega)\exp(-ix_0/v_r), \tag{104}$$

where D is a constant dislocation. The exponential phase factor corresponds to a unilateral rupture in the x direction with speed v_r. Chouet (1982) treats the problem of an expanding circular tensile crack, and in I_F he uses

$$s(r, \theta, \omega) = (D/i\omega)\exp(-i\omega r/v_r), \tag{105}$$

where r and θ are a cylindrical coordinate system with the origin at the center of the crack. For this choice of s, I_F can also be integrated analytically. For some choices of s, the integration over one dimension of the fault can be done analytically, whereas the other dimension must be integrated numerically. Chouet (1981), studying a fluid driven tensile fracture, uses an opening function that varies with x_0 but is independent of z_0:

$$s(x_0, z_0, t) = D(x_0, t), \tag{106}$$

where $D(x_0, t)$ is the output from a 2D finite-difference simulation of the fracture process. In this case the analytic integral over z_0 is straightforward, but the integral over x_0 must be performed numerically. Chouet performs that integral by using the rectangle rule quadrature. Other applications of this technique can be found in Chouet (1983, 1985). An alternative method for such integrals might be a generalized Filon method (Frazer and Gettrust, 1984).

Equation (102) and analogous equations give us the source-induced Φ and Ψ at depths z_{s-1} and z_s. We can use Eqs. (33) and (39) to write the source terms needed in Eq. (89),

$$\mathbf{b}_s^0(z_{s-1}) = D_P\mathbf{v}(z_{s-1}) \tag{107}$$

and

$$\mathbf{b}_s^0(z_s) = D_P\mathbf{v}(z_s), \tag{108}$$

where

$$\mathbf{v}(z_{s-1}) = [\Phi^+(z_{s-1}), \Psi^+(z_{s-1}), 0, 0]^T, \tag{109}$$

and

$$\mathbf{v}(z_s) = [0, 0, \Phi^-(z_s), \Psi^-(z_s)]^T. \tag{110}$$

The component $\Psi^{\pm}$ of Ψ associated with the P–SV propagation having wave number $\mathbf{k}$ is the component of Ψ lying in the x–y plane perpendicular

to **k** (Fig. 3):

$$\Psi_{y'} = (k_x\Psi_y - k_y\Psi_x)/k, \tag{111a}$$

$$\Psi^+ = \Psi_{y'}(z_{s-1}), \tag{111b}$$

$$\Psi^- = \Psi_{y'}(z_s). \tag{111c}$$

Here, Φ^+ is given by evaluating Eq. (102) for $z = z_{s-1}$, and Φ^- is obtained from Eq. (102) with $z = z_s$.

The derivation of $\mathbf{b}_s^0$ for the SH problem is slightly different from that for the P–SV problem, because it is not necessary to use the SH form of Eq. (33) to transform from potentials to displacement. If we denote the components of SH displacement above and below the source as $u_{y'}^+$ and $u_{y'}^-$, respectively, then

$$u_{y'}^{\pm} = i[k\Psi_z \pm (\gamma/k)(k_x\Psi_x + k_y\Psi_y)] \tag{112}$$

(Bouchon, 1979, Eq. (23)), and

$$\mathbf{b}_s^0(z_{s-1}) = u_{y'}^+[1, i\mu_s\gamma_s]^T, \tag{113}$$

$$\mathbf{b}_s^0(z_s) = u_{y'}^-[1, -i\mu_s\gamma_s]^T \tag{114}$$

(Chouet, 1987).

A final comment is warranted on the evaluation of the Fourier transform over the wave number (Eq. 79). Any of a variety of quadrature rules could be used (Frazer and Gettrust, 1984). Bouchon and Aki (1977) and Bouchon (1979) use the rectangle rule quadrature to convert Eq. (79) to the form

$$\mathbf{u}_d(x, y, z, \omega) \approx \left[4\pi^2/L_xL_y\right] \sum_{n_x=-\infty}^{\infty} \sum_{n_y=-\infty}^{\infty} \mathbf{K}_F(n_x, n_y), \tag{115}$$

where

$$\mathbf{K}_F(n_x, n_y) = \mathbf{u}(k_x, k_y, z, \omega)\exp(-ik_xx - ik_yy), \tag{116}$$

$$k_x = 2\pi n_x/L_x, \qquad k_y = 2\pi n_y/L_y, \tag{117}$$

and where the d subscript indicates the result of a discrete sum. Their conversion of the continuous integral to a discrete sum has interesting properties. In this particular problem, use of the rectangle rule happens to give the exact answer to a different but related physical problem, one in which there is a grid of identical sources separated by distances L_x and L_y in the x and y directions. Consequently $\mathbf{u}_d(x, y, z, t)$ will be identically equal to the result for a single source $\mathbf{u}(x, y, z, t)$ for times t up until the wave from the nearest multiple source arrives at the observer. Hence, this time can be made arbitrarily large by choosing L_x and L_y sufficiently large.

Another way to look at the properties of the discrete sum is to recognize that Eq. (79) is a spatial Fourier transform because of the exponential term. By using the sum, Eq. (115), we are implicitly saying that $\mathbf{K}_F(k_x, k_y)$ is a sum of Dirac delta functions of the form $\sum\sum\delta(k_x - 2\pi n_x/L_x)\delta(k_y - 2\pi n_y/L_y)$, where k_x and k_y are continuous variables. Hence its Fourier transform must be periodic in space. The use of the discrete transform is in no way necessary for including the effects of an extended source.

The conversion from integrals over k_x and k_y to the discrete sum can be performed at any stage in the derivation. We have delayed its introduction until after derivation of the potentials from the extended source; Bouchon and Aki (1977) and Bouchon (1979) introduced it earlier and expressed the point force potentials Φ^x, Ψ^x; Φ^y, Ψ^y; and Φ^z, Ψ^z as discrete sums. The actual evaluation of the sum is the last step in obtaining the extended-source seismograms.

From the standpoint of extended-source modeling, the most useful consequence of this method of inverse transformation is that it yields the ground motions at a dense grid in x and y of observer locations. By contrast, all of the implicit and explicit Green's function integration methods we have previously discussed yield ground motions at a small set of observer locations. Hence, this method would be quite useful for studies of ground motions over large regions (Bouchon, 1980a,b; Chouet, 1981, 1983, 1985).

III. Examples of Finite Fault Calculations

A. Haskell Model in a Whole Space

Although a Haskell model of rupture occurring in a uniform whole space was never considered, even by Haskell himself, to be a realistic model of an earthquake, it conveniently illustrates a few of the principles presented earlier. Figure 11 shows our test geometry. The fault is a 1 km × 1 km square lying in the x_1–x_2 plane, centered on $x_1 = 0$, $x_2 = 0$. The rupture front is a line parallel to the x_2 axis, and it advances at a uniform velocity in the $+x_1$ direction. The slip vector is uniform everywhere and is parallel to the x_1 axis. Five observer locations are considered: two in the forward direction ($\mathbf{F}_1$ and $\mathbf{F}_2$), two normal to the fault ($\mathbf{N}_1$ and $\mathbf{N}_2$), and one in the backward direction (**B**). Except when stated otherwise, rupture velocity in all these examples is 3.0 km/sec, slip velocity is 1.0 cm/sec, rise time is 0.12 sec, and the medium parameters are $\alpha = 6.0$ km/sec, $\beta = 3.4$ km/sec, and $\rho = 2.5$ gm/cm^3.

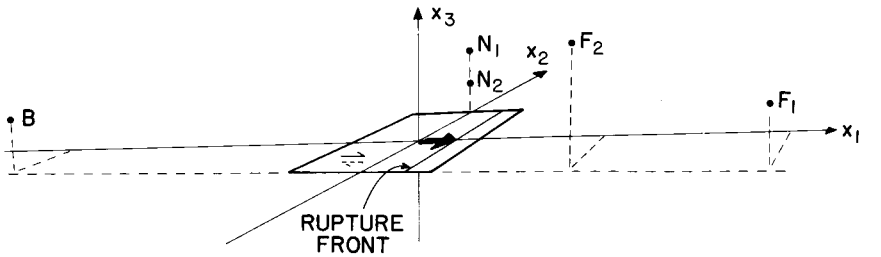

FIG. 11. Geometry of fault and observer locations $\mathbf{F}_1$ (3.0, −0.5, 0.5), $\mathbf{F}_2$ (1.5, −0.5, 1.0), $\mathbf{N}_1$ (0, 0.5, 0.43), $\mathbf{N}_2$ (0, 0.5, 0.2), and $\mathbf{B}$ (−3.0, −0.5, 0.5) for a Haskell model in a wholespace. The fault is 1 km × 1 km and lies in the x_1–x_2 plane. The rupture front is a line parallel to the x_2 axis that advances with constant velocity in the $+x_1$ direction. Slip is parallel to the x_1 axis and has constant amplitude on the fault.

1. Point-Source Summation

The characteristic behavior of the point-source summation method becomes immediately obvious if we examine the form of **s** and **T** on the fault surface. Suppose we wish to simulate our Haskell model by using a grid of 30 × 30 point sources on the fault and using the form of the representation theorem, Eq. (15). For an observer at $\mathbf{F}_1$ and for $\omega = 20\pi$ sec^{-1}, $\mathrm{Re}[T_1^1(\mathbf{x}, \omega; \mathbf{F}_1, 0)]$ is shown in Fig. 12, sampled on the 30 × 30 grid. Because the Green's function is dominated by the far-field S wave at this

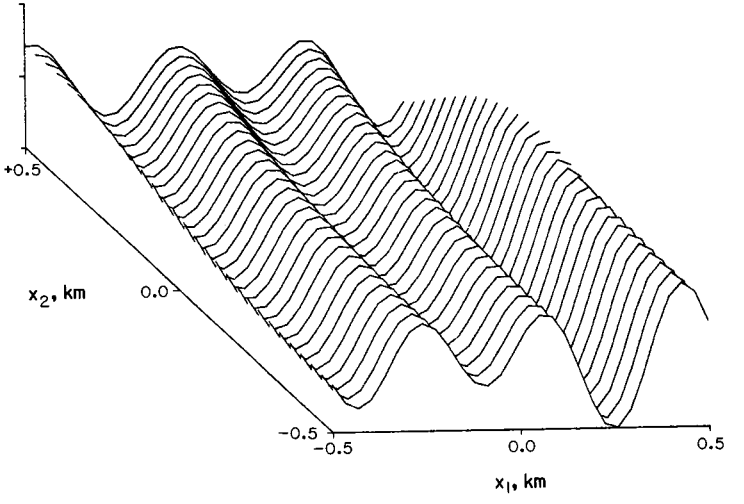

FIG. 12. Real part of the x_1 component of traction resulting on the fault in Fig. 11 caused by the application of a point force in the x_1 direction at the observer at $\mathbf{F}_1$. The result shown is the 10-Hz spectral component, evaluated on a square grid of 900 points on the fault.

distance, the traction should be of the form of Eq. (46), and lines of equal travel time should be lines of equal phase. Consequently, we expect the lines of equal phase to form circles concentric about $\mathbf{F}_1$, which is what Fig. 12 shows. Slip **s** is of the form of Eq. (45), with lines of equal phase being lines of equal rupture time (Fig. 13). The dot product of these two functions, i.e., the integrand of Eq. (14) is shown in Fig. 13. As promised in Section II.C.1 for an observer in the forward direction, the integrand is smoother than either **s** or **T**. It is well sampled by the 30 × 30 grid, and

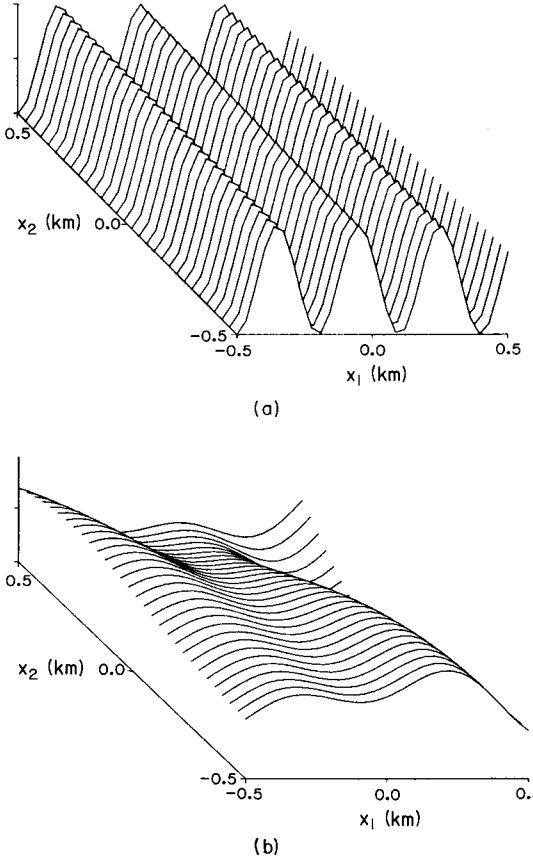

FIG. 13. (a) Real part of the 10-Hz component of the slip spectrum, shown as a function of position on the fault. The rupture front is a line that advances at 3.0 km/sec left to right. (b) Real part of the product of the function shown in (a) with the traction function of Fig. 12. This scalar function is integrated over the fault surface to obtain the 10-Hz component of the ground-motion spectrum at $\mathbf{F}_1$. The functions in (a) and (b) are both evaluated on a square grid of 900 points, which is sufficiently dense to represent **sT** accurately.

consequently it can be integrated accurately by the midpoint rule. If we drop the rupture velocity to 1.0 km/sec, both **s** and **s** • **T** become considerably more oscillatory, and the 30 × 30 grid no longer provides an adequate sampling of **s** • **T** (Fig. 14). The sparse sampling leads to an inaccurate quadrature result. In the time domain seismograms, these numerical inaccuracies are manifested as individual pulses from each of the point sources. These inaccuracies are greater for observers in the backward direction than for those in the forward direction (Fig. 15). As mentioned earlier, the numerical errors associated with point-source summations first become

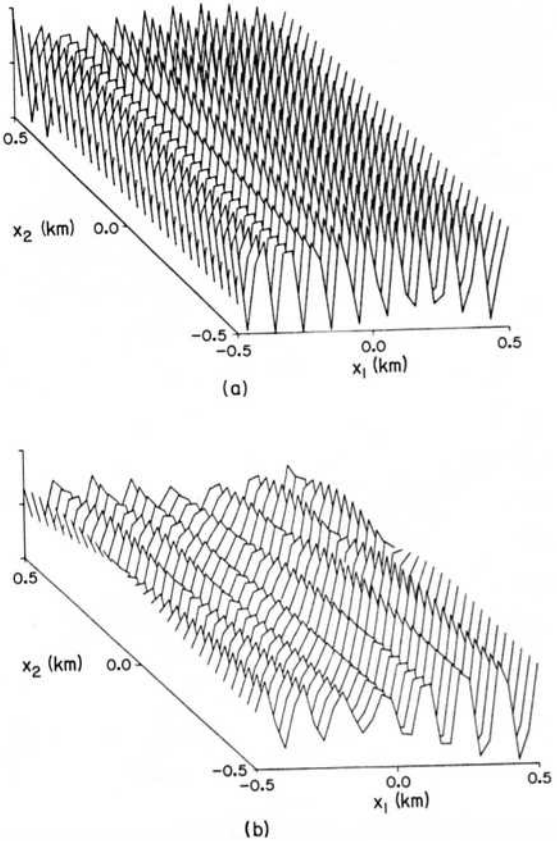

FIG. 14. (a) The same as panel (a) in Fig. 13 but for a 1.0 km/sec rupture velocity. Note that the spatial wavelength of the function is much shorter and that it is undersampled by the 900 point grid. (b) The real part of the product of the function shown in (a) with the traction function of Fig. 12. This product is undersampled solely because of the poor sampling of the slip function.

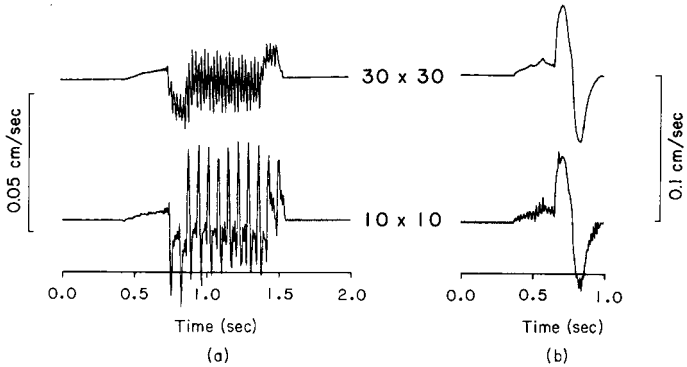

FIG. 15. Particle velocity in the x_3 direction at observer locations **B** (a) and $\mathbf{F}_2$ (b), calculated by point-source summation in the frequency domain. These seismograms are unfiltered and are calculated in the 0–63 Hz band. Seismograms in the upper row are calculated for a square grid of 900 point sources on the fault; those in the lower row are for a grid of 100 point sources. The effect of discrete point sources is much more apparent in the backward direction (observer at **B**, Fig. 11) than in the forward direction ($\mathbf{F}_2$).

evident at high frequencies. At low frequencies, for which the integrands have long spatial wavelengths, the point source summation can be quite accurate, as can be seen for the flatness of the zero levels in the seismograms in Fig. 15.

2. Adaptive Integration

The inaccuracies of a point-source summation generally result from the undersampling of **s**. In Fig. 12 it is clear that the grid of 900 points is quite adequate for sampling **T** at 10 Hz regardless of the rupture velocity. Although it may be necessary to calculate **s** and **s** • **T** on a much denser grid to assure an accurate result, values of **T** on an arbitrarily dense grid can be obtained by bilinear interpolation between the sample points shown in Fig. 12. Consider momentarily an example calculation concocted to exacerbate the problems of point-source summation. We again use a Haskell model in a whole space, but we boost the medium velocities to $\alpha = 7.0$ km/sec, $\beta = 4.0$ km/sec, and $\rho = 2.8$ gm/cm^3. We drop the rupture velocity to 0.6 km/sec and shorten the rise time to 0.01 sec. Seismograms calculated in the 0–10 Hz band for observers at $\mathbf{F}_2$, $\mathbf{N}_1$, and **B** (Fig. 11) are shown in Fig. 16. The discreteness of the 16×16 grid of point sources is apparent at all azimuths but especially in the backward direction. If the adaptive sampling rules, Eqs. (64) and (65), are used with $m = n = 6$, **T** is calculated on a 5×5 grid and **s** on a 6×6 grid at the lowest frequencies. At 10 Hz **T** is calculated on a 16×16 grid, and **s** is calculated on a 104×104 grid. By

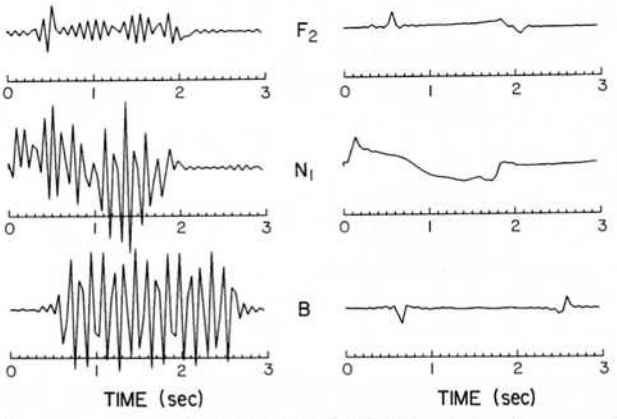

FIG. 16. The x_3 component of velocity in the 0–10-Hz band for observers at $\mathbf{F}_2$, $\mathbf{N}_1$, and $\mathbf{B}$ (Fig. 11) for a 0.6 km/sec rupture velocity. The left column consists of seismograms calculated by point-source summation of a grid of 16 × 16 sources. The seismograms in the right column result from summations in which the number of grid points was adjusted for each frequency to ensure 6 grid points per wavelength. The traction function was sampled on a 5 × 5 grid at the lowest frequency and on a 16 × 16 grid at the highest frequency. The slip function was sampled on a 6 × 6 grid at the lowest frequency and a 104 × 104 grid at the highest frequency. Such dense sampling of s was necessitated by the very low rupture velocity.

using an adaptive grid, a much more accurate answer is obtained at high frequencies, compared to a point-source summation, and $\mathbf{T}$ is evaluated ~ 50% fewer times. Because the adaptive technique attempts to distribute errors equally over the entire frequency band, at low frequencies the adaptive technique is less accurate than the point-source summation in this case. This feature can be seen by examining the seismograms for the observer at $\mathbf{N}_1$ after 2 sec in Fig. 16.

3. A Haskell Model and Far-Field Green's Functions

In Section II.C.1 we used far-field ray theory Green's functions with kinematic rupture models to obtain high-frequency seismograms in the near-source region of a fault. We now show an example of such a calculation for an observer at $\mathbf{N}_2$ (Fig. 11). The observer at $\mathbf{N}_2$ is well within one source dimension of the fault. In this example we return to the original test problem except that the rise time is 0.1 sec. Figure 17 compares the isochrone integration with a frequency-domain point-source summation using only the R^{-1} terms (discarding the R^{-2} and R^{-4} terms) for a dislocation in a whole space [Aki and Richards, 1980, Eq. (4.30)]. The isochrone-integration seismogram is unfiltered, and the point-source summation seismogram is bandpass filtered from 0 to 30 Hz using a zero

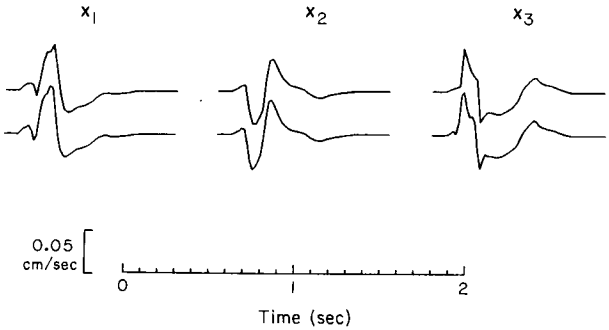

FIG. 17. Demonstration that the isochrone integration technique yields the exact result for far-field Green's functions in the near-source region of a fault. The three columns contain seismograms for the x_1, x_2, and x_3 components of velocity at observer N_2 (Fig. 11). The upper trace of each pair is the isochrone integration result obtained directly in the time domain. The lower trace of each pair is the result obtained by frequency domain summation of a 30 × 30 grid of point sources (far-field terms only). The lower traces have been filtered by a filter that is flat in the 0–20-Hz band and has a cosine-squared rolloff in the 20–30-Hz band. Only the R^{-1} radiation terms for a point dislocation have been used in the lower traces.

phase-shift filter having a cosine-squared ($\cos^2$) taper from 20 to 30 Hz. The two results are essentially identical except for minor differences caused by the filtering of the point-source summation result. In this example the magnitude of the neglected R^{-2} and R^{-4} terms is comparable to that of the R^{-1} term.

B. More Complicated Sources in a Vertically Inhomogeneous Medium

1. Comparisons Between Ray Theory and Exact Seismograms

Because the isochrone integration method using ray theory can be so much faster computationally than methods using complete Green's functions, it is worthwhile to investigate its performance in situations more realistic than a Haskell model in a whole space. Bernard and Madariaga (1984) have compared ray theory seismograms to synthetic seismograms calculated by Bouchon (1982) to simulate the Gilroy 6 recording of the 1979 Coyote Lake earthquake (Fig. 18). Bouchon's synthetics were calculated by a point-source summation of complete Green's functions for the layered medium. While the ray theory result lacks the near-field wave that causes the long-period ramp before the arrival of the S wave from the origin, the far-field term reproduces the 2.5-sec-long main pulse surprisingly

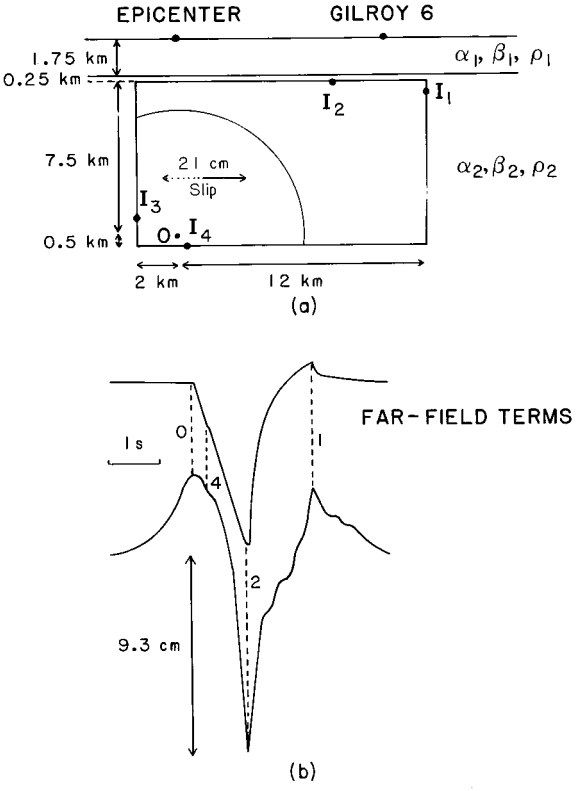

FIG. 18. Comparison of isochrone integration seismograms and complete seismograms for a simulation of the 1979 Coyote Lake earthquake. (a) Test geometry. A vertical section of the earth containing the fault is shown. The earth model consists of a uniform layer overlying a uniform half-space containing the fault, where O is the hypocenter. The rupture front is an expanding circle limited by the edges of the rectangular fault. I_1, I_2, I_3, and I_4 are critical points where isochrones touch the edges of the fault, thus radiating high-frequency pulses. Displacement, perpendicular to the fault, is calculated at station Gilroy 6. (b) The upper trace (asymptotic method) is the result of isochrone integration (far-field terms). The lower trace [Bouchon's method (1982)] is the result of point-source summation of complete Green's functions, including all near-field terms. Here, 0, 1, 2, and 4 show the locations of S pulses associated with the hypocenter and critical points.

well. Its higher frequency features correlate with those in the complete seismogram, as they should.

In the next example, we show what may be one of the most significant limitations on the use of ray theory for extended-source calculations. Ray theory does not correctly predict the phase shifts, diffracted P wave, and whispering gallery mode that in some cases accompany an SV wave

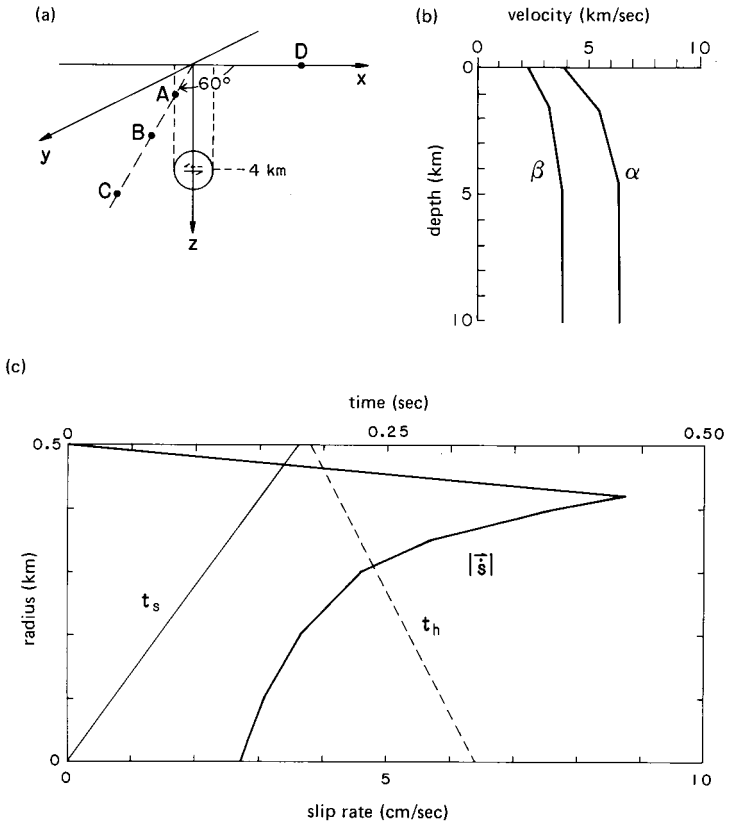

FIG. 19. (a) Test geometry. A circular fault 1 km in diameter with its center at a depth of 4 km lies in the x–z plane. Observers at **A**, **B**, and **C** are located in the x–y plane (free surface) at an azimuth 60° off strike, at epicentral distances of 2.0, 5.0, and 10.0 km, respectively. Observer **D** is at an epicentral distance of 5.0 km along strike. (b) The earth velocity structure consists of two gradient zones overlying a uniform half-space (Table I). (c) The slip model is pure strike-slip and is circularly symmetric about the hypocenter. Rupture time is shown by (——), healing time (– – –), and slip rate (——). Note that the fault slips for 0.32 sec at its center and 0.01 sec at its periphery.

incident at the free surface (Spudich and Frazer, 1984). The test situation, Fig. 19, largely mimics that of Campillo and Bouchon (1983). Rupture initiates at a 4-km depth and expands uniformly to fill a circle of 0.5-km radius. Healing then initiates at the periphery and propagates inward to the origin. In our case the slip-rate time function is a rectangle (see Section II.A) rather than the Kostrov function used by Campillo and Bouchon. The slip-rate, rupture time, and healing time on the crack as a function of radius

TABLE I. EARTH MODEL PARAMETERS[a]

Depth (km)	α(km/sec)	β(km/sec)	ρ(g/cm^3)
0.0	4.0	2.3	2.6
1.5	5.5	3.2	2.8
4.5	6.3	3.65	2.9
∞	6.3	3.65	2.9

[a]Linear interpolation is used to derive model parameters for depths not given in this table.

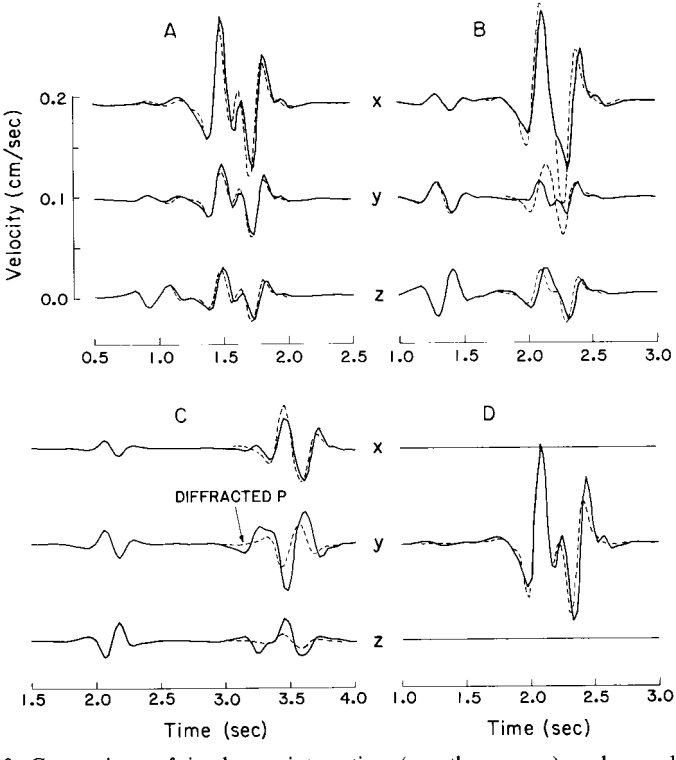

FIG. 20. Comparison of isochrone integration (ray theory, ----) and complete (——) mograms for the test in Fig. 19, for observers at **A** (r = 2 km), **B** (r = 5 km), **C** (r = 10 , and **D** (r = 5 km). All seismograms have been band pass filtered from 1–10 Hz using a causal filter. The three components of ground velocity are shown for each observer. The P es agree well at all observers, and S waves agree well at short distance (**A**) and where only energy is present (**D**); S-wave discrepancies are apparent at **B** and **C** due to phase shifts, diffracted SP wave, and a whispering gallery mode associated with SV waves incident at free surface. These effects are not included in the ray theory result.

are shown in Fig. 19. Slip everywhere on the fault is parallel to the x axis. Our earth model is given in Table I. Figure 20 shows the x, y, and z components of ground velocity observed at **A**, **B**, **C**, and **D** in Fig. 19. The dashed line is the ray theory result, and the solid line is the result obtained using the adaptive integration method of Spudich (1981) and complete Green's functions calculated with the DWFE method of Olson *et al.* (1984). All seismograms have been bandpass filtered from 1 to 10 Hz using a zero phase-shift filter having a cosine ($\cos^1$) taper from 1 to 3 Hz and from 7 to 10 Hz. The ray theory result was obtained using about 1% of the computer time required for the complete result. The two methods agree quite well at **A** (2-km epicentral distance), showing that the near-field term is not important in this case. The P waves match well at all epicentral distances, but the S-wave match deteriorates at **B** and **C** due to the complexities associated with SV at the free surface. A diffracted P wave, preceding the S wave, can be seen at 3.2 sec in the y and z components at observer **C**. These discrepancies are clearly associated with the SV wave because the ray theory S wave at observer **D**, which is on an SV node, agrees well with the complete synthetic.

These examples show that ray theory works very well when used within its range of validity. Because the largest motions in earthquakes are generally associated with S waves, future work in ray theory should concentrate upon finding a solution for the SV problems, which does not affect the simplicity of the isochrone formalism.

2. Modeling Strong Motion Records from the 1979 Imperial Valley Earthquake

In this section we discuss some of the numerical considerations involved in a realistic extended-source calculation. The example we will use is from the work of Archuleta (1984), who determined a faulting model consistent with the data for the 1979 Imperial Valley earthquake using DWFE (Olson *et al.*, 1984) to calculate the Green's functions and the adaptive method of Spudich (1981) to evaluate the fault surface integral. We will not dwell on the source parameters or the interpretation of the model, all of which are found in Archuleta (1984).

The objective was to find a rupture model that predicted synthetic seismograms consistent with the data. The data were the three-component particle velocity records at 16 stations, all within 23 km of the Imperial Valley fault. The medium had a well-determined P-wave velocity structure and a reasonably well-determined S-wave velocity structure (see Table II). The fault had a length of at least 35 km and a downdip width of 13 km. Faulting at the surface was primarily right-lateral strike-slip with a minor amount of dip-slip motion.

TABLE II. ELASTIC PARAMETERS FOR THE IMPERIAL VALLEY[a]

Depth (km)	α(km/sec)	β(km/sec)	ρ(g/cm^3)
0.0	1.70	0.40	1.8
0.4	1.80	0.70	1.8
5.0	5.65	3.20	2.5
11.0	5.85	3.30	2.8
11.0	6.60	3.70	2.8
12.0	7.20	4.15	2.8

[a]Between any two successive depths linear interpolation is used to determine intermediate values. A half-space exists for depths greater than 12 km. Different elastic parameters at the same depth indicate a discontinuity.

The basic numerical constraints on generation of the Green's functions using the DWFE method were determined by five parameters: the maximum length of time of the synthetics ($t_{\max}$), the maximum frequency of interest ($f_{\max}$), the maximum distance between any observer and the most distant point on the fault ($r_{\max}$), the maximum P-wave velocity in the medium ($\alpha_{\max}$), and the minimum shear-wave velocity in the medium ($\beta_{\min}$). For the Imperial Valley data, Archuleta (1984) selected the following values: $t_{\max} = 30$ sec, $f_{\max} = 1.0$ Hz, $r_{\max} = 35$ km, $\alpha_{\max} = 7.2$ km/sec, and $\beta_{\min} = 0.4$ km/sec.

The first step of the problem is to obtain traction Green's functions $\mathbf{T}$ on a grid of points on the fault. This grid must be sufficiently dense to allow accurate integration of $\dot{\mathbf{s}} \cdot \mathbf{T}$ over the fault surface. As mentioned earlier, the DWFE method obtains expansion coefficients $U(z_i, t_j, k)$, $V(z_i, t_j, k), \ldots, T(z_i, t_j, k)$, $i = 1, \ldots, N_z$, $j = 1, \ldots, N_t$, where N_z is the number of mesh points and N_t is the number of time steps, by using a finite-element technique to solve the time-domain form of Eqs. (21) and (22) for each wave number k. The DWFE method adjusts its mesh spacing Δz in depth to give 6 mesh points per shortest shear wavelength:

$$\Delta z(z) = \beta(z)/(6f_{\max}), \tag{118a}$$

$$z_i = \sum_{j=1}^{i} \Delta z(z_{j-1}), \qquad z_0 = 0, \qquad i = 1, \ldots, N_z. \tag{118b}$$

Because traction Green's functions are ultimately calculated at the depths $\{z_i\}$, this variable spacing is completely consistent with the sampling criterion of Eq. (64). For the Imperial Valley case, with a fault extending to a 13-km depth, Green's functions for depth z_i with $1 \le i \le 22$ were calculated and saved. A time step of about 0.015 sec was chosen to satisfy

the Courant stability criterion for the finite-element calculation and to give $N_t = 2048$ for a 30-sec-long time series.

The maximum number of wave numbers is simply

$$N_k = k_{\max}/\Delta k, \tag{119}$$

where

$$k_{\max} = 2\pi f_{\max}/(0.9\beta_{\min}), \tag{120}$$

and

$$\Delta k \approx 2\pi/R_{\max}, \tag{121}$$

where

$$R_{\max} = (\alpha_{\max} t_{\max} + r_{\max})/2. \tag{122}$$

The quantity $(0.9\beta_{\min})$ represents the minimum phase velocity of interest, the velocity of the fundamental mode Rayleigh wave in the shallowest part of the medium. If the time window of interest does not include such slowly traveling waves, then the number of wave numbers can be reduced appropriately. Here, $R_{\max}$ represents the radius at which a reflecting boundary must be placed such that reflected energy from this boundary does not arrive within the time window $[0, t_{\max}]$ being synthesized. Substituting the values used for the Imperial Valley, we found $N_k = 348$. In practice, DWFE optimizes itself in the course of the computation so that this number is the upper limit with the actual number of wave numbers being less, especially if the fault surface does not penetrate into the lowest velocity ($\beta_{\min}$) material.

The computation of U, V, W, P, S, and T and their Fourier transformation into the frequency domain required 3.5 hr of computation time (all computation times will be those measured on a VAX11/780 with a VMS operating system). The components U, V, W, P, S, and T are saved as functions of (z, k, ω). The number of frequencies N_f saved after transforming to the frequency domain is simply $f_{\max}/\Delta f$ where $\Delta f = 1.0/t_{\max}$. Thus, only 31 frequencies, including zero frequency, are saved. The advantage of saving $U, \ldots, T$ in the z, k, ω domain is that they embody the exact medium response. Green's functions for any epicentral distance and point-force orientation can be obtained from them by use of Eq. (19). The disadvantage is the amount of storage, amounting to approximately $6N_f N_k N_z$ complex words (about 1.5 million in this case).

The next step in the procedure is to calculate for all observers the tractions $\mathbf{T}^m(\mathbf{x}, \omega; \mathbf{y}_i, 0)$, as in Eq. (15), where m is the point-force direction, $\mathbf{x}$ is the position on the fault, and $\mathbf{y}_i$ is the location of observer i. This is accomplished by using Eqs. (19) and (20) and by further differentiating the displacements to get strains, from which are derived stresses and tractions.

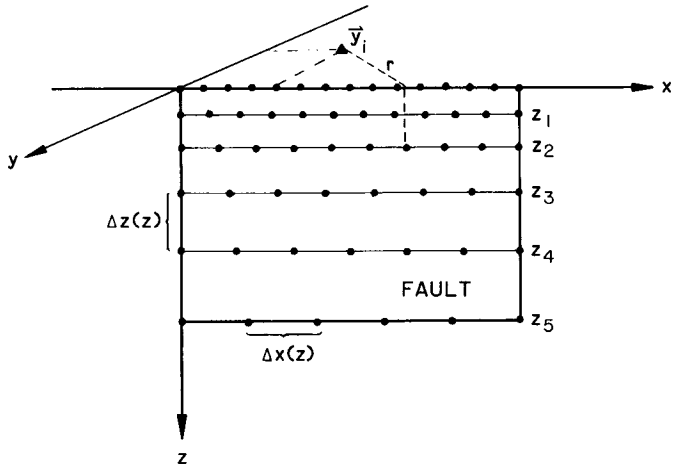

FIG. 21. Spacing of sample points x_T where T is sampled on the fault, and $z_0, z_1, \ldots,$ are the depths at which $U, V, \ldots, T$ are obtained using DWFE. Horizontal spacing of sample points varies with local S-wave velocity, which is a function of depth (Table II). Here, y_i is the location of observer i, and r is the cylindrical radius for which Eq. (19) must be evaluated to obtain the traction at the indicated point.

Here, $\mathbf{T}$ is calculated on a variably spaced mesh of points on the fault, in accordance with Eq. (64). For simplicity we assume the fault lies in the x–z plane (Fig. 21), and we let $\mathbf{x}_{ij} = x_i\hat{\mathbf{x}} + z_j\hat{\mathbf{z}}$ be the ijth traction sample point on the fault. The grid depths used by DWFE in Eq. (118b) are $\{z_j\}$ and

$$\Delta x(z, f) = \beta(z)/6f, \tag{123a}$$

$$x_i = \sum_{j=1}^{i} \Delta x(z_{j-1}, f), \qquad z_0 = 0. \tag{123b}$$

This leads to a horizontal spacing of points on the fault that varies as a function of frequency and depth. For each of the observers used by Archuleta (1984), the evaluation of $\mathbf{T}$ (e.g., Fig. 22) for all $\mathbf{x}_{ij}$ and all frequencies took about 2 hr of CPU time, and storage of $\mathbf{T}$ required about 0.4 million complex words, which were saved for use with subsequent slip models.

The slip rate function was specified using four parameters: strike-slip rate amplitude, dip-slip rate amplitude, slip duration, and rupture time, on a 182-point grid that was spaced equally every 2.5 km along-strike and 1.0-km downdip. Thus, each faulting model consisted of 728 independent parameters. This grid of 182 points was not the same as the grid of quadrature points $\{x_{s_j}\}$ (Section II.C.3.a). The sample spacing in both x

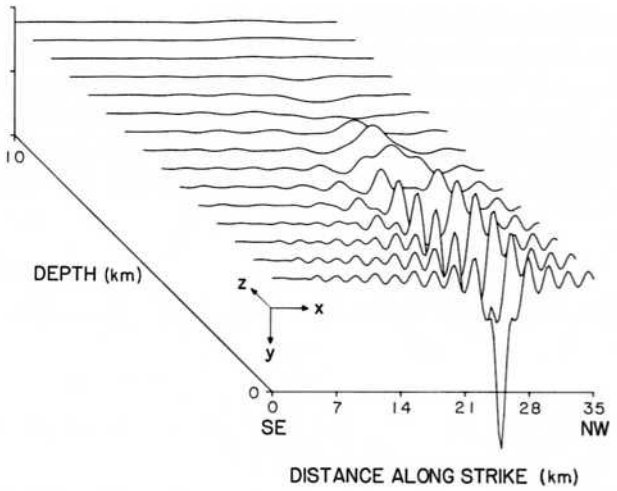

FIG. 22. Real part of the x component of traction resulting on the Imperial fault from the application of a point force at $x = 24.9$ km, $y = -1.0$ km, corresponding to Station E07 of the El Centro array (Archuleta, 1984). The 0.51-Hz component of the traction spectrum is shown. Because the point force is quite close to the fault, the traction peaks strongly nearest the point force. The wavelength of the traction is smallest at zero depth, where the shear velocity is minimum, and the wavelength increases with depth.

and z for the quadrature is given by Eq. (65). Using $f = 0.5$ Hz and $m = 8$, on the shallowest part of the fault the rupture velocity might be 0.5 km/sec, implying a 0.125-km spacing for quadrature points. Deeper on the fault, where the rupture velocity might be 3.0 km/sec, the quadrature point spacing is about 0.75 km. Because quadrature points almost never coincide with the 182 points upon which the rupture model parameters are specified, the four rupture parameters are obtained at quadrature points by bilinear interpolation. The spectrum of the slip rate, $\dot{\mathbf{s}}(\mathbf{x}_s, \omega)$ is easily calculated from the four interpolated parameters. The integration of the product of the Green's function and slip model ($\dot{\mathbf{s}} \cdot \mathbf{T}$) over the fault for 31 frequencies required 15 min of computation time per observer. Because it is generally insufficient to determine the validity of a particular rupture model by looking at the resulting synthetic seismograms at only one observer, synthetic seismograms were calculated at a minimum of six observers for each rupture model. Thus, each model took about 1.5 hr of CPU time.

While the initial computation time needed to obtain U, V, W, P, S, and T can be large, in fact, the inverse Bessel transform for each observer required nearly the same amount of time. The actual computation time for doing the integration and inverse Fourier transform to compute a particle velocity at a given observer is rather small by comparison. However, in the

trial-and-error procedure of trying to find agreement between the synthetics and the data, it may take a large number (~ 300 in the case of the Imperial Valley earthquake) of trial rupture models before a satisfactory fit is found. In this case, the total computation time for the integration over the fault plane becomes the costly part of the problem. Although the overall computation time is nontrivial, synthetics, which incorporate the vertical hetero-

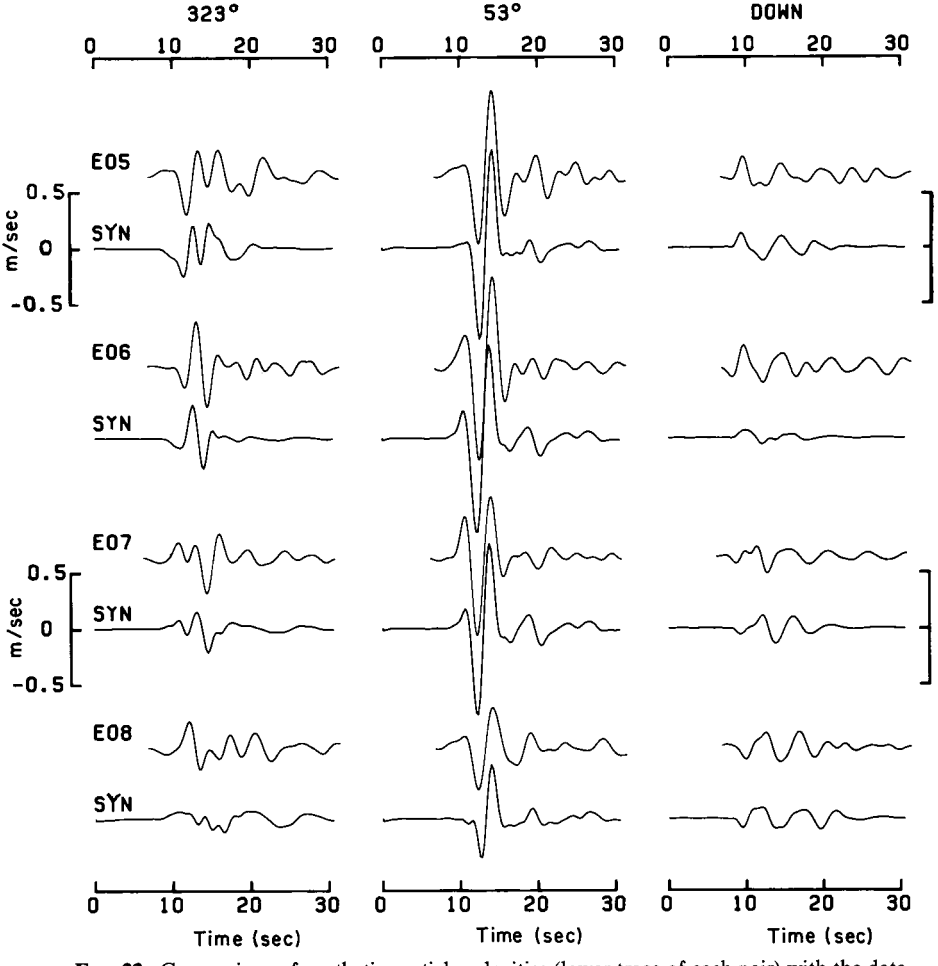

FIG. 23. Comparison of synthetic particle velocities (lower trace of each pair) with the data for Stations E05, E06, E07, and E08. Each column represents a different component of motion. The 323° and the 53° are the horizontal components with positive motion directed along the azimuth, measured clockwise from north. The data and synthetics have been filtered to 0.5 Hz. (From Archuleta, 1984; published by the American Geophysical Union.)

geneity of the velocity structure and the spatial and temporal finiteness of the faulting, can be computed that are in agreement with the data (Fig. 23).

ACKNOWLEDGMENTS

The authors wish to thank Dr. Bernard Chouet for his explanations on the inner workings of his and Dr. Bouchon's methods. Drs. Chouet, S. H. Hartzell, and T. H. Heaton provided helpful reviews of this paper. We thank Dr. Allen Olson for allowing us to use and modify his DWFE code.

This research was supported, in part, by the Office of Nuclear Regulatory Research, U.S. Nuclear Regulatory Commission.

REFERENCES

Aki, K. (1967). *J. Geophys. Res.* **72**, 1217–1231.
Aki, K. (1968). *J. Geophys. Res.* **73**, 5359–5376.
Aki, K., and Richards, P. G. (1980). "Quantitative Seismology: Theory and Methods." Freeman, San Francisco, California.
Alekseev, A. S., and Mikhailenko, B. G. (1980). *J. Geophys.* **48**, 161–172.
Anderson, J. G., and Richards, P. G. (1975). *Geophys. J. R. Astron. Soc.* **42**, 347–373.
Andrews, D. J. (1981). *J. Geophys. Res.* **86**, 10821–10834.
Apsel, R. J., and Luco, J. E. (1983). *Bull. Seismol. Soc. Am.* **73**, 931–952.
Apsel, R. J., Frazier, G. A., Jurkevics, A., and Fried, J. C. (1981). *Geol. Surv. Open-File Rep. (U.S.)* No. 81-276.
Archuleta, R. J. (1984). *J. Geophys. Res.* **89**, 4559–4585.
Archuleta, R. J., and Day, S. M. (1980). *Bull. Seismol. Soc. Am.* **70**, 671–689.
Archuleta, R. J., and Frazier, G. A. (1978). *Bull. Seismol. Soc. Am.* **68**, 541–572.
Archuleta, R. J., and Hartzell, S. H. (1981). *Bull. Seismol. Soc. Am.* **71**, 939–957.
Bache, T. C., Day, S. M., and Swanger, H. J. (1982). *Bull. Seismol. Soc. Am.* **72**, 15–28.
Backus, G., and Mulcahy, M. (1976a). *Geophys. J. R. Astron. Soc.* **46**, 341–361.
Backus, G., and Mulcahy, M. (1976b). *Geophys. J. R. Astron. Soc.* **47**, 301–329.
Bernard, P., and Madariaga, R. (1984). *Bull. Seismol. Soc. Am.* **74**, 539–558.
Boatwright, J. (1981). *Bull. Seismol. Soc. Am.* **71**, 69–94.
Boatwright, J. (1982). *Bull. Seismol. Soc. Am.* **72**, 1049–1068.
Boore, D. M., and Joyner, W. B. (1978). *Bull. Seismol. Soc. Am.* **68**, 283–300.
Bouchon, M. (1979). *J. Geophys.* **84**, 3609–3614.
Bouchon, M. (1980a). *J. Geophys. Res.* **85**, 356–366.
Bouchon, M. (1980b). *J. Geophys. Res.* **85**, 367–375.
Bouchon, M. (1981). *Bull. Seismol. Soc. Am.* **71**, 959–971.
Bouchon, M. (1982). *Bull. Seismol. Soc. Am.* **72**, 745–759.
Bouchon, M., and Aki, K. (1977). *Bull. Seismol. Soc. Am.* **67**, 259–277.
Bracewell, R. (1965). "The Fourier Transform and Its Applications." McGraw-Hill, New York.
Burridge, R., and Knopoff, L. (1964). *Bull. Seismol. Soc. Am.* **54**, 1875–1888.
Cabrera, J. J., and Levy, S. (1984). *Geophysics* **49**, 1915–1932.
Campillo, M., and Bouchon, M. (1983). *Bull. Seismol. Soc. Am.* **73**, 83–96.

Červený, V., and Klimeš, L. (1984). *Geophys. J. R. Astron. Soc.* **79**, 119–134.
Červený, V., Klimeš, L., Pleinerová, V., and Pšenčík, I. (1987). *Geophys. J. R. Astron. Soc.* Submitted.
Chapman, C. H. (1978). *Geophys. J. R. Astron. Soc.* **54**, 481–518.
Chapman, C. H., and Orcutt, J. A. (1985). *Rev. Geophys.* **23**, 105–164.
Chin, R. C. Y., Hedstrom, G., and Thigpen, L. (1984a). *J. Comput. Phys.* **54**, 18–56.
Chin, R. C. Y., Hedstrom, G., and Thigpen, L. (1984b). *Geophys. J. R. Astron. Soc.* **77**, 483–502.
Chouet, B. (1981). *J. Geophys. Res.* **86**, 5985–6016.
Chouet, B. (1982). *J. Geophys. Res.* **87**, 3868–3872.
Chouet, B. (1983). *J. Volcanol. Geotherm. Res.* **19**, 367–379.
Chouet, B. (1985). *J. Geophys. Res.* **90**, 1881–1893.
Chouet, B. (1987). *Bull. Seismol. Soc. Am.* Submitted.
Cormier, V. F. (1980). *Bull. Seismol. Soc. Am.* **70**, 691–716.
Cormier, V. F., and Beroza, G. C. (1987). *Bull. Seismol. Soc. Am.* Submitted.
Day, S. M. (1977). Ph.D. Thesis, Univ. of California, San Diego.
Day, S. M. (1982). *Bull. Seismol. Soc. Am.* **72**, 1881–1902.
Dunkin, J. W. (1965). *Bull. Seismol. Soc. Am.* **55**, 335–358.
Farra, V., Bernard, P., and Madariaga, R. (1986). *In* "Earthquake Source Mechanics," (S. Das, J. Boatwright, and C. Scholz, eds.), pp. 121–130. Geophys. Monogr. 37 of the Am. Geophys. Union, Washington, D.C.
Frazer, L. N., and Gettrust, J. F. (1984). *Geophys. J. R. Astron. Soc.* **76**, 461–481.
Frazer, L. N., and Sen, M. K. (1985). *Geophys. J. R. Astron. Soc.* **80**, 121–147.
Gay, N. C., and Ortlepp, W. D. (1974). *Bull. Geol. Soc. Am.* **90**, Part I, 47–58.
Gilbert, F., and Dziewonski, A. (1975). *Philos. Trans. R. Soc. London, Ser. A* **278**, 187–269.
Haddon, R. A., and Buchen, P. W. (1981). *Geophys. J. R. Astron. Soc.* **67**, 587–598.
Hartzell, S. (1978). *Geophys. Res. Lett.* **5**, 1–4.
Hartzell, S. (1982). *Bull. Seismol. Soc. Am.* **72**, 2381–2388.
Hartzell, S., and Heaton, T. (1983). *Bull. Seismol. Soc. Am.* **73**, 1553–1583.
Hartzell, S., and Heaton, T. (1986). *Bull. Seismol. Soc. Am.* **76**, 649–674.
Hartzell, S., and Helmberger, D. (1982). *Bull. Seismol. Soc. Am.* **72**, 571–596.
Hartzell, S., Frazier, G., and Brune, J. (1978). *Bull. Seismol. Soc. Am.* **68**, 301–316.
Haskell, N. A. (1964). *Bull. Seismol. Soc. Am.* **54**, 1811–1841.
Haskell, N. A. (1966). *Bull. Seismol. Soc. Am.* **56**, 125–140.
Heaton, T. H. (1982). *Bull. Seismol. Soc. Am.* **72**, 2037–2062.
Heaton, T. H., and Helmberger, D. V. (1979). *Bull. Seismol. Soc. Am.* **69**, 1311–1341.
Helmberger, D. V., and Harkrider, D. G. (1978). *In* "Modern Problems in Elastic Wave Propagation" (J. Miklowitz and J. D. Achenbach, eds.), pp. 499–518. Wiley, New York.
Helmberger, D. V., and Malone, S. (1975). *J. Geophys. Res.* **80**, 4881–4888.
Imagawa, K., Mikami, N., and Mikumo, T. (1984). *J. Phys. Earth* **32**, 317–338.
Irikura, K. (1983). *Bull. Disaster Prev. Inst., Kyoto Univ.* **33**, 63–104.
Izutani, Y. (1981). *J. Phys. Earth* **29**, 537–558.
Joyner, W. B., and Boore, D. M. (1986). *In* "Earthquake Source Mechanics," (S. Das, J. Boatwright, and C. Scholz, eds.), pp. 269–274. Geophys. Monogr. 37 of the Am. Geophys. Union, Washington, D.C.
Julian, B. R. (1983). *Nature (London)* **303**, 323–325.
Kanamori, H. (1979). *Bull. Seismol. Soc. Am.* **69**, 1645–1670.
Kennett, B. L. N. (1980). *Geophys. J. R. Astron. Soc.* **61**, 1–10.
Kennett, B. L. N. (1983). "Seismic Wave Propagation in Stratified Media." Cambridge Univ. Press, London and New York.

Kennett, B. L. N., and Illingworth, M. R. (1981). *Geophys. J. R. Astron. Soc.* **66**, 633–675.
Kind, R. (1979). *J. Geophys.* **45**, 373–380.
King, G. C. P. (1983). *Pure Appl. Geophys.* **121**, 761–816.
Kostrov, B. V. (1964). *J. Appl. Math. Mech.* (*Engl. Transl.*) **28**, 1077–1087.
Koyama, J. (1985). *Tectonophysics* **118**, 227–242.
Liu, H.-L., and Helmberger, D. V. (1983). *Bull. Seismol. Soc. Am.* **73**, 201–218.
Liu, H.-L., and Helmberger, D. V. (1985). *Bull. Seismol. Soc. Am.* **75**, 689–708.
Madariaga, R. (1976). *Bull. Seismol. Soc. Am.* **66**, 639–666.
Maruyama, T. (1963). *Tokyo Daigaku Jishin Kenkyusho Iho* **41**, 467–486.
Munguia, L., and Brune, J. N. (1984). *Geophys. J. R. Astron. Soc.* **79**, 747–771.
Olson, A. H., and Apsel, R. J. (1982). *Bull. Seismol. Soc. Am.* **72**, 1969–2002.
Olson, A. H., Orcutt, J. A., and Frazier, G. A. (1984). *Geophys. J. R. Astron. Soc.* **77**, 421–460.
Robinson, K. (1951). *J. Appl. Phys.* **22**, 1045.
Sen, M. K., and Frazer, L. N. (1985). *Geophys. J. R. Astron. Soc.* **82**, 415–438.
Sibson, R. H. (1980). *J. Geophys. Res.* **85**, 6239–6247.
Sibson, R. H. (1986). *Annu. Rev. Earth Planet. Sci.* **14**, 149–175.
Spudich, P. (1980). *Geophys. Res. Lett.* **7**, 717–720.
Spudich, P. (1981). *EOS Trans. Am. Geophys. Union* **62**, 960.
Spudich, P., and Ascher, U. (1983). *Geophys. J. R. Astron. Soc.* **75**, 101–124.
Spudich, P., and Frazer, L. N. (1984). *Bull. Seismol. Soc. Am.* **74**, 2061–2082.
Spudich, P., and Oppenheimer, D. (1986). *In* "Fifth Maurice Ewing Symposium on Earthquake Source Mechanics," Series 6 (S. Das, J. Boatwright, and C. Scholz, eds.), pp. 285–296. Am. Geophys. Union, Washington, D.C.
Tchalenko, J. S. (1970). *Bull. Geol. Soc. Am.* **81**, 1625–1640.
Tchalenko, J. S., and Ambraseys, N. N. (1970). *Bull. Geol. Soc. Am.* **81**, 41–60.
White, S. H. (1973). *Nature* (*London*) **244**, 276–278.
Yao, Z. X., and Harkrider, D. G. (1983). *Bull. Seismol. Soc. Am.* **73**, 1685–1699.